DOI: https://doi.org/10.14256/JCE.1573.2016

Građevinar 12/2022

Primljen / Received: 20.1.2016.
Ispravljen / Corrected: 27.10.2016.
Prihvaćen / Accepted: 11.1.2017.
Dostupno online / Available online: 10.1.2023.

Effect of near-fault ground motion with pulse signal on dynamic response of dam-reservoir-foundation systems

Authors:

Prof. **Ahmet Can Altunisik**, PhD. CE
Karadeniz Technical University, Trabzon, Turkey
Department of Civil Engineering
ahmetcan8284@hotmail.com
Corresponding author

Assist.Prof. **Hasan Sesli**, PhD. CE
Yalova University, Yalova, Turkey
Department of Civil Engineering
hasan_sesli@hotmail.com

Professional paper

Ahmet Can Altunisik, Hasan Sesli

Effect of near-fault ground motion with pulse signal on dynamic response of dam-reservoir-foundation systems

This paper aimed to determine the effects of a pulse signal of near-fault ground motion on the dynamic response of gravity dams, including dam-reservoir-foundation interaction, using different reservoir modelling approaches such as Westergaard, Lagrange, and Euler. As a case study, a Sarıyar concrete gravity dam located on the Sakarya River, 120 km northeast of Ankara, was considered for investigating the near-fault ground-motion pulse effects on dam responses. First, the main principles and basic formulations of these approaches were presented. Then, finite element models of the dam were realized considering dam-reservoir-foundation interaction using ANSYS software. To determine the structural response of the dam under pulse effects of the near-fault ground motion, linear transient analyses were performed using the 1999 Taiwan Chi-Chi and 1979 Imperial Valley ground motions, which display apparent velocity pulses as representative of the near-fault earthquakes. Subsequently, the dynamic characteristics were compared to demonstrate the models of the fluid domain effects and pulse signal effects.

Key words:

concrete gravity dam, dam-reservoir-foundation interaction, hydrodynamic pressure, near-fault ground motion

Stručni rad

Ahmet Can Altunisik, Hasan Sesli

Učinak pomaka tla s impulsnim signalom uslijed bliskih potresa na dinamički odziv sustava brana – akumulacija – temelj

U ovom radu cilj je utvrditi učinke impulsnih pomaka tla uslijed bliskih potresa na dinamički odgovor gravitacijskih brana uključujući i interakciju brana – akumulacija – temelj na različite pristupe modeliranju akumulacije kao što su Westergaardov, Lagrangeov i Eulerov pristup. Kao studija slučaja, betonska gravitacijska brana Sarıyar smještena na rijeci Sakarya, 120 km sjeveroistočno od Ankare, odabrana je za istraživanje učinaka impulsnog pomaka tla uslijed bliskog potresa na odziv brane. Prvo su izložena glavna načela i osnovna formulacija pristupa. Zatim su uspostavljeni modeli brane s konačnim elementima uzimajući u obzir interakciju brana-akumulacija-temelj, pomoću računalnog programa ANSYS., sve da bi se odredio strukturni odgovor brane pod utjecajem impulsnog pomaka tla. Linearne privremene analize provedene su korištenjem Taiwan Chi-Chi 1999. i Imperial Valley 1979. koji prikazuju prividne impulse brzine kao reprezentativne za bliske potrese. Na kraju analize uspoređene su dinamičke karakteristike sve kako bi se demonstrirali modeli učinaka domene fluida i učinaka impulsnog signala.

Ključne riječi:

betonska gravitacijska brana, interakcija brana-akumulacija-temelj, hidrodinamički tlak, bliski potres

1. Introduction

Dams are important engineering structures subjected to fluid-structure interactions, which have contributed to the development of civilisation for a long time. Concrete gravity dams have also been built to meet the increasing demands for power, irrigation, drinking water, etc. They are often constructed in seismically prone areas. However, their failure can cause an irreparable loss of life and property.

The dam–reservoir interaction and hydrodynamic pressures acting on the dam face are important factors affecting the dynamic response of concrete gravity dams during earthquakes. The consideration of these factors is important, particularly in the case of earthquake dynamic loads. Three approaches are generally used in the analyses of dam–reservoir interactions. The simplest approach is the Westergaard approach (added mass approach) presented by Westergaard in 1933 [1]. Another is the Lagrange approach, in which the response of the dam and reservoir is expressed using displacements only. Therefore, specific interfacial equations are not essential [2-7]. The third method for representing the reservoir-dam interaction is the Euler approach, in which the structure and fluid motions are expressed with displacements and pressures [8]. There are numerous studies in the literature on the static and dynamic behaviour of dams considering dam-reservoir-foundation interactions using different FSI approaches [9-23].

Strong ground motions are the most important dynamic problems for the stability and safety of concrete gravity dams. Earthquakes can be significantly different in the near-fault region compared to a distance far away from the epicentre (far-field earthquakes). The main characteristics of these impulse motions are the period and maximum velocity pulse amplitudes. The velocity pulse has specific characteristics of near-fault earthquakes that cannot be observed in far-field earthquakes [24].

Near-fault ground motions recorded in recent earthquakes (1989 Loma Prieta, 1994 Northridge, 1995 Japan Hyogoken-Nanbu, 1999 Taiwan Chi-Chi) are characterised by a large velocity pulse, which exposes the structure to high input energy at the beginning of the earthquake. These pulses are strongly influenced by the orientation of the fault, direction of the slip, and location of the recording station relative to the fault, referred to as the directivity effect due to the propagation of the rupture toward the recording site [25-29].

Ground motions recorded within the near-fault region by stations located in the direction of the fault rupture qualitatively differ from the usual far-fault earthquake ground motion. The ground motion recorded in the near-fault region displayed a long-period pulse in the acceleration history, appearing as a coherent pulse in the velocity and displacement time histories. Such a pronounced pulse does not exist in the ground motions recorded at locations outside the near-fault region [30].

Pomaci tla bliskih potresa mogu se klasificirati kao pomaci s Near-fault ground motions can be classified as those with or without a pulse signal. The velocity waveforms were chosen to identify the pulse signals because it is easier to detect the pulse from the velocity [27, 30]. Owing to these unique characteristics of near-fault ground motions, the seismic responses of civil engineering structures, such as buildings, tunnels, bridges, nuclear stations, dams, towers, viaducts, wind turbines, and tanks, under near-fault ground motions have received a great deal of attention over the last decades [5, 7, 11, 24, 28, 30, 32-49].

From the literature review, it can be seen that there are insufficient studies on the effects of near-fault ground motions with pulse signals on the dynamic response of gravity dams applied in different reservoir modelling approaches. This paper presents the effects of near-fault ground motion with pulse signals on the dynamic response of gravity dams using the Westergaard, Lagrange, and Euler approaches. The Sarıyar concrete gravity dam, located on the Sakarya River, 120 km northeast of Ankara, was selected as a case study. The finite element model of the dam was constructed considering the dam-reservoir-foundation interaction using ANSYS software. The 1999 Taiwan Chi-Chi and 1979 Imperial Valley ground motion records displaying a ground motion with an apparent velocity pulse were selected to represent the near-fault earthquake. These near-fault ground motions are referred to as those obtained in the vicinity of a fault with an apparent velocity pulse (pulse duration longer than 1.0 s), distance to the fault of less than 10 km, and peak ground velocity/peak ground acceleration (PGV/PGA) ratio larger than 0.1 s. For comparison, ground motion recorded from the same earthquakes without an initial pulse was considered to determine the pulse effect on the dynamic response of concrete gravity dams. From the analyses, the dynamic characteristics, maximum displacements, maximum-minimum principal stresses, and maximum-minimum principal strains were retained for comparison to demonstrate the FSI and pulse signal effects.

2. Formulation

2.1. Westergaard (added mass) approach

The added mass approach was presented for the first time by Westergaard in 1933 [1]. In this approach, the dam was assumed to be rigid, semi-infinite, and with a vertical upstream surface. Surface waves in the fluid were neglected. The distribution of the hydrodynamic pressure along the upstream surface following the earthquake was substituted with the initial forces of the lumped masses attached to the interface. Individual masses were added to the nodes of the finite-element mesh along the upstream surface of the dam. Figure 1 depicts the variation in hydrodynamic pressure with depth.

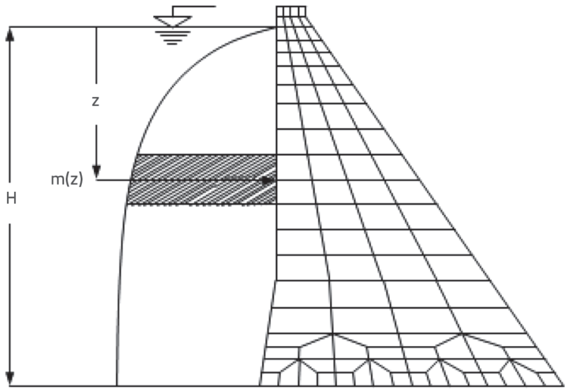

Figure 1. Distribution of hydrodynamic pressure on finite mesh

Individual masses are given according to Figure 1 as:

$$m(z)=\frac{7}{8}\frac{w}{g}\sqrt{Hz} \tag{1}$$

Where m(z) is the mass distribution as a function of the depth of the reservoir, w is the unit weight of water, g is the acceleration due to gravity, and H and z are the depths of water from the surface.

2.2. Lagrange approach

In the Lagrange approach, the response of the dam and reservoir is expressed by displacements, and specific interface equations are not essential [2, 3]. The formulation of the fluid system based on this approach can be found in literature [50]. The fluid was assumed to be linearly elastic, inviscid, and with an irrotational flow field. For a general three-dimensional reservoir, stress-strain relationships can be written in matrix form as:

$$\begin{Bmatrix} P \\ P_x \\ P_y \\ P_z \end{Bmatrix} = \begin{bmatrix} C_{11} & 0 & 0 & 0 \\ 0 & C_{22} & 0 & 0 \\ 0 & 0 & C_{33} & 0 \\ 0 & 0 & 0 & C_{44} \end{bmatrix} \begin{Bmatrix} \varepsilon_v \\ w_x \\ w_y \\ w_z \end{Bmatrix} \tag{2}$$

gdje su P_x, P_g, P_z rotacijska naprezanja; C_{22}, C_{33}, C_{44} parametri where P_x, P_y, and P_z are rotational stresses; C_{22}, C_{33}, and C_{44} are constraint parameters; w_x, w_y and w_z are rotations about the Cartesian axes x, y, and z, respectively; and P, C_{11}, and ε_v are pressures which are equal to the mean stresses, bulk modulus, and volumetric strain of the fluid, respectively. The fluid irrotationality is considered by means of the penalty method [51], and the rotation and constraint parameters are included in the stress-strain equation (Eq. 2) of the fluid.

In this study, the equations of motion of the fluid system were obtained using the potential and kinetic energy principles. Using the finite element method, the total strain energy of the fluid system can be written as:

$$\pi_e = \frac{1}{2}\mathbf{U}_f^T\mathbf{K}_f\mathbf{U}_f \tag{3}$$

where $\mathbf{U}_f$ and $\mathbf{K}_f$ are the vectors of nodal displacements and stiffness matrix of the fluid system, respectively. $\mathbf{K}_f$ was obtained by summing the stiffness matrices of the fluid elements, as:

$$\left.\begin{aligned} \mathbf{K}_f &= \sum \mathbf{K}_f^e \\ \mathbf{K}_f^e &= \int_V \mathbf{B}_f^{eT}\mathbf{C}_f\mathbf{B}_f^e dV^e \end{aligned}\right\} \tag{4}$$

where $\mathbf{C}_f$ is an elasticity matrix consisting of diagonal terms given in Eq. (2), and $\mathbf{B}_f^e$ is the strain-displacement matrix of the fluid element. An important characteristic of fluid systems is their ability to displace without a change in the volume. For reservoir and storage tanks, this movement is known as sloshing waves, in which the displacement is in the vertical direction. The increase in the potential energy of the system owing to the free surface motion can be written as:

$$\pi_s = \frac{1}{2}\mathbf{U}_{sf}^T\mathbf{S}_f\mathbf{U}_{sf} \tag{5}$$

where $\mathbf{U}_{sf}$ is the vertical nodal displacement vector and $\mathbf{S}_f$ is the stiffness matrix of the free surface of the fluid system. $\mathbf{S}_f$ is obtained by the sum of the stiffness matrices of the free-surface fluid elements, as :

$$\left.\begin{aligned} \mathbf{S}_f &= \sum \mathbf{S}_f^e \\ \mathbf{S}_f^e &= \rho_f g \int_A \mathbf{h}_s^T\mathbf{h}_s dA^e \end{aligned}\right\} \tag{6}$$

where $\mathbf{h}_s$ is a vector consisting of interpolation functions of the free-surface fluid element, ρ_f is the mass density of the fluid, and g is the acceleration due to gravity. The kinetic energy of the system can be written as:

$$T = \frac{1}{2}\dot{\mathbf{U}}_f^T\mathbf{M}_f\dot{\mathbf{U}}_f \tag{7}$$

where $\dot{\mathbf{U}}_f^T$ is the nodal velocity vector and $\mathbf{M}_f$ is the mass matrix of the fluid system. $\mathbf{M}_f$ can be obtained by summing the mass matrices of the fluid elements:

$$\left.\begin{aligned} \mathbf{M}_f &= \sum \mathbf{M}_f^e \\ \mathbf{M}_f^e &= \rho_f \int_V \mathbf{H}^T\mathbf{H} dV^e \end{aligned}\right\} \tag{8}$$

where $\mathbf{H}$ is a matrix comprising interpolation functions of the fluid element. Combining Eqs. (3), (5), and (7) using Lagrange's equation [52], the following is obtained:

$$\mathbf{M}_f\ddot{\mathbf{U}}_f + \mathbf{K}_f^*\mathbf{U}_f = \mathbf{R}_f \tag{9}$$

where, $\mathbf{K}_f^*$, $\ddot{\mathbf{U}}_f$ and $\mathbf{R}_f$ are the system stiffness matrix including the free surface stiffness, the nodal acceleration vector and time-varying nodal force vector for the fluid system, respectively. Reduced integration orders were utilized in the formation of the fluid element matrices.

The equations of motion for the fluid system (Eq. (9) have a form similar to that of the structural system. Determination of the interface condition is required to obtain the coupled equations of the fluid-structure system. Because the fluid was assumed to be inviscid, only the displacement in the direction normal to the interface was continuous at the interface of the system. Assuming that the positive face is the structure and the negative face is the fluid, the boundary condition at the fluid-structure interface is:

$$U_n^- = U_n^+ \tag{10}$$

where U_n is the normal component of the interface displacement [53]. Using the interface condition, the equation of motion of the coupled system to ground motion, including the damping effects, is given by:

$$\mathbf{M}_c\ddot{\mathbf{U}}_c + \mathbf{C}_c\dot{\mathbf{U}}_c + \mathbf{K}_c\mathbf{U}_c = \mathbf{R}_c \tag{11}$$

where $\mathbf{M}_c$, $\mathbf{C}_c$, and $\mathbf{K}_c$ are the mass, damping, and stiffness matrices for the coupled system, respectively, and $\mathbf{U}_c$, $\dot{\mathbf{U}}_c$, $\ddot{\mathbf{U}}_c$ and $\mathbf{R}_c$ are the vectors of the displacements, velocities, accelerations, and external loads of the coupled system, respectively.

2.3. Euler approach

The Euler approach is widely used in the finite and boundary element analyses of dams considering fluid-structure interaction. In this approach, the structure and fluid motions are expressed by displacements and pressures, respectively. Both the structure and fluid move jointly based on the fluid-structure interface. Hence, specific interface equations must be identified. The three-dimensional motion of a linear compressible, non-viscous, and non-rotational fluid under small displacements is referred to as the following wave equation [54, 55],

$$P_{,xx} + P_{,yy} + P_{,zz} = \frac{1}{C^2}P_{,tt} \tag{12}$$

where x, y, and z are Cartesian coordinates, t is time, C represents the pressure wave velocity of the fluid, and $P_{,xx}$, $P_{,yy}$, $P_{,zz}$ are the second derivatives of hydrodynamic pressure for variables x, y, and z, respectively. The hydrodynamic pressures in the fluid were obtained from the appropriate boundary conditions for Eq. (12), given by:

$$P = 0 \text{ (if not surface waves on a free surface)} \tag{13}$$

$$P = \rho g u_{sf} \text{ (if there are surface waves on the free surface)} \tag{14}$$

$$P_{,n} = \rho u_n \text{ (for fluid-structure interface)} \tag{15}$$

where ρ, n, u_n and u_{sf} are the mass density of the fluid, normal to the fluid surface for the fluid-structure interface, acceleration in the normal direction, and displacement of the fluid free surface in the vertical direction, respectively. Fluid surface waves were not considered in this study, and the finite element equations of motion for the fluid system and the dynamic motion of the medium have the following forms:

$$\left[M_f^p\right]\left\{\ddot{P}\right\} + \left[K_f^p\right]\left\{P\right\} = -\rho\left[R\right]^T\left\{\ddot{U}_{fs}\right\} \tag{16}$$

$$\left[M_s\right]\left\{\ddot{U}_s\right\} + \left[C_s\right]\left\{\dot{U}_s\right\} + \left[K_s\right]\left\{U_s\right\} = \left\{F\right\} + \left\{F_{fs}\right\} \tag{17}$$

where $[M_f^p]$, $\{\ddot{P}\}$, $[K_f^p]$, {P}, [R], $\{\ddot{U}_{fs}\}$, $[M_s]$, $[C_s]$, $[K_s]$, $\{\ddot{U}_s\}$, $\{\dot{U}_s\}$, $\{U_s\}$, {F} and $\{F_{fs}\}$ are the fluid mass matrix, second derivative of the hydrodynamic pressure vector for time, stiffness matrix, hydrodynamic pressure vector, fluid-structure interface matrix, and structure accelerations in the fluid-structure interface, mass matrix, damping matrix, stiffness matrix, acceleration vector, velocity vector, displacement vector, external load vector, and additional external load vector on the structure from hydrodynamic pressures in fluid, respectively. In addition, $\{F_{fs}\}$ is expressed as $\{F_{fs}\}$ = [R]{P}.
By combining Eqs. (16) and (17), a common equation of motion can be obtained for fluid-structure interaction.

3. Near-fault ground mMotions

Near-fault ground motions can be classified as those with or without a pulse signal. The velocity waveforms were chosen to identify the pulse signals because it is easier to detect the pulse from the velocity. The velocity time series is shown in Figure 2 for a comparison of the near-fault ground motion with and without the pulse signal.

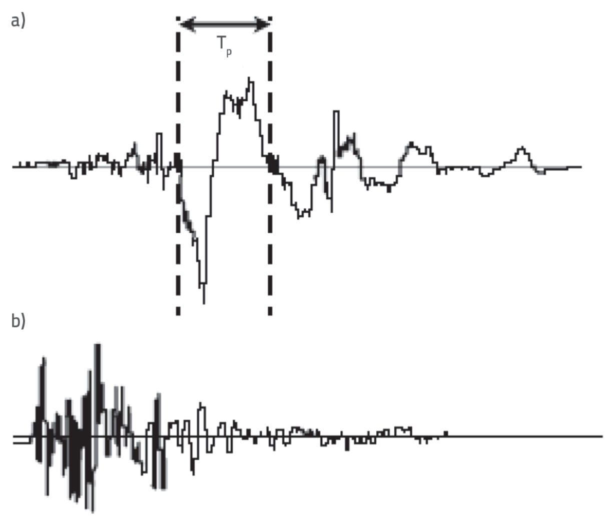

Figure 2. Velocity time series: a) with pulse signal; b) without pulse signals

Near-fault ground motion records selected as an input excitation with pulse characteristic were the 1999 Taiwan Chi-Chi (TCU053EW) and 1979 Imperial Valley (E06230) earthquakes. In addition, another set of earthquake records recorded from the same earthquake events was selected to illustrate far-fault ground motion without pulse characteristics: TCU120EW

Table 1. Properties of selected near-fault and far-fault ground motion records

Ground motion	Earthquake	Component	PGA [m/s²]	PGV [cm/s]	PGV/PGA [s]	Mw*	Distance to fault [km]
With pulse	1999 Chi-Chi	TCU053EW	0.229g	39.6	0.176	7.62	5.95
Without pulse	1999 Chi-Chi	TCU120EW	0.228g	59.8	0.264	7.62	9.0
With pulse	1979 Imperial Valley	IMPVALL-E06230	0.449g	113.5	0.258	6.53	1.35
Without pulse	1979 Imperial Valley	IMPVALL-E08230	0.466g	52.1	0.114	6.53	3.86
Mw* - earthquake magnitude according to Richter scale							

and E08230. These records were applied in the upstream-downstream direction which is the first mode direction to attain more sensitive and reliable results. The vertical and longitudinal directions of these earthquakes were neglected in the linear elastic dynamic analysis. The ground motion records were obtained from the PEER strong-motion database [56]. This database contains information on the site conditions and soil type of the instrument locations. The PGA, PGV, epicentral distances from the site to the fault, projection on the surface, and PGV/PGA ratios are given in Table 1.

Near-fault ground motions with the same peak acceleration values were selected for a more accurate comparison of the results. If the ground-motion records had different peak accelerations, the comparison would not be straightforward.

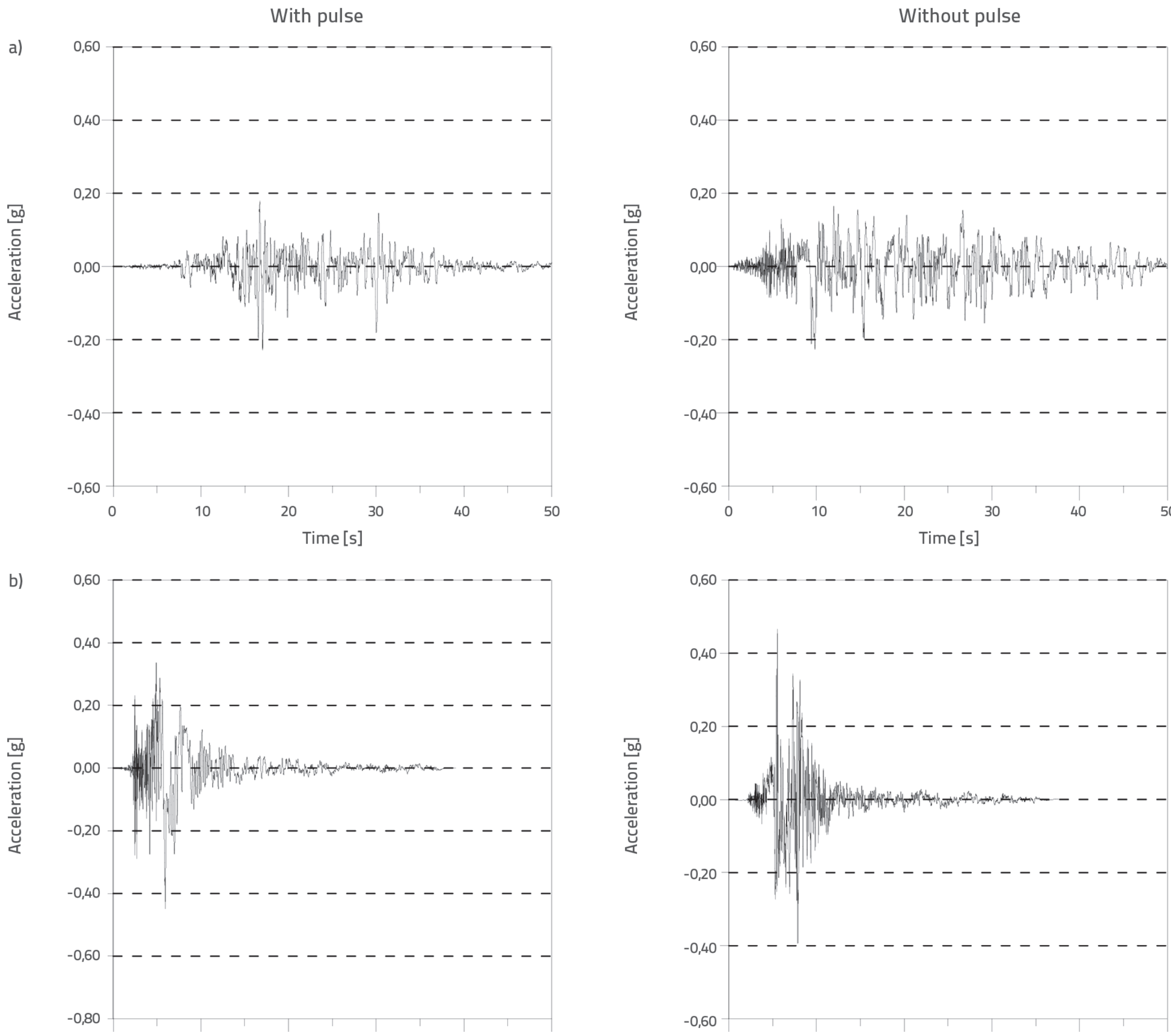

Figure 3. Acceleration time histories of near-fault and far-fault ground motions obtained from: a) 1999 Taiwan Chi-Chi; b) 1979 Imperial Valley earthquakes

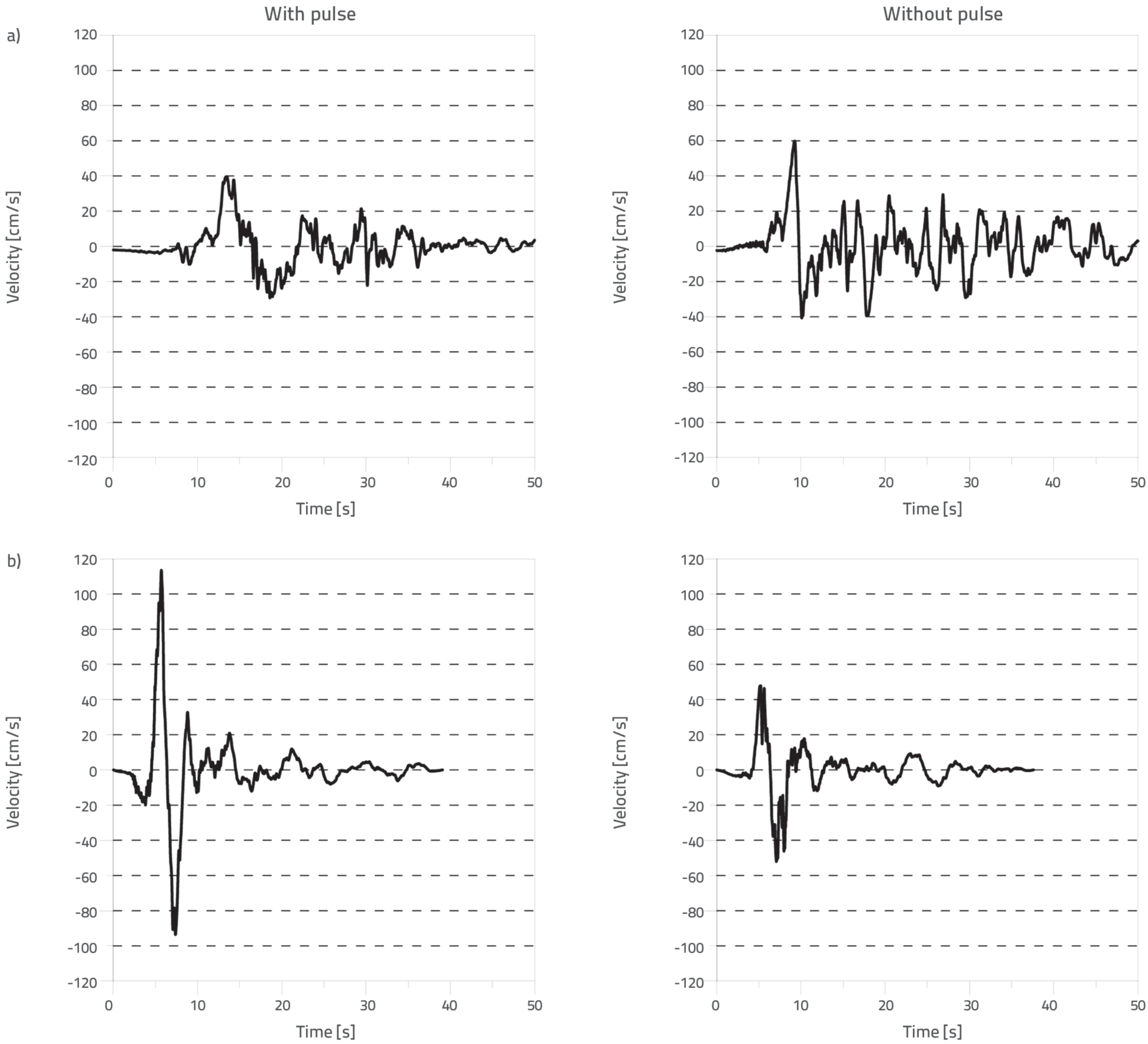

Figure 4. Velocity-time histories of near-fault and far-fault ground motions obtained from: a) 1999 Taiwan Chi-Chi; b) 1979 Imperial Valley earthquakes

The acceleration and velocity-time histories of the near-fault ground motions with and without a pulse are presented in Figures 3 and 4, respectively. Only the effective 50-s duration was considered to decrease the time necessary for the computations.

4. Numerical example

The Sarıyar concrete gravity dam (Figure 5a) was chosen for analyses to determine and compare the effects of pulse-like near-fault ground motions on the structural dynamic response of concrete gravity dams, including dam-reservoir-foundation interaction, using different modelling approaches such as Westergaard (added masses), Lagrange (displacement-based), and Euler (pressure-based) for the hydrodynamic pressure. The Sarıyar Dam is located on the Sakarya River, 120 km northeast of Ankara, Turkey. A dam was built to generate electrical power. The crest length and width are 257 and 7 m, respectively. The maximum reservoir height is 85 m. The dimensions of the dam are shown in Figure 5b. The finite element models of the dam, including dam-reservoir-foundation interaction using the Westergaard, Lagrange, and Euler approaches, were realized in the ANSYS program and are depicted in Figure 6.

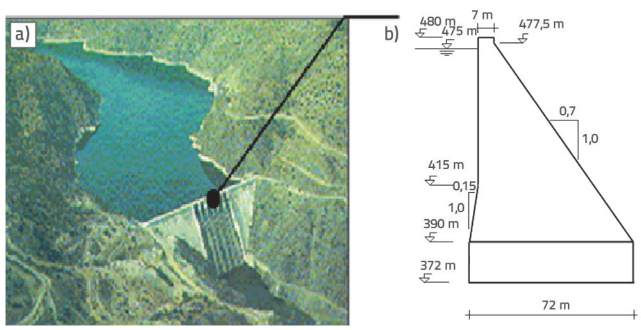

Figure 5. Sarıyar concrete gravity dam

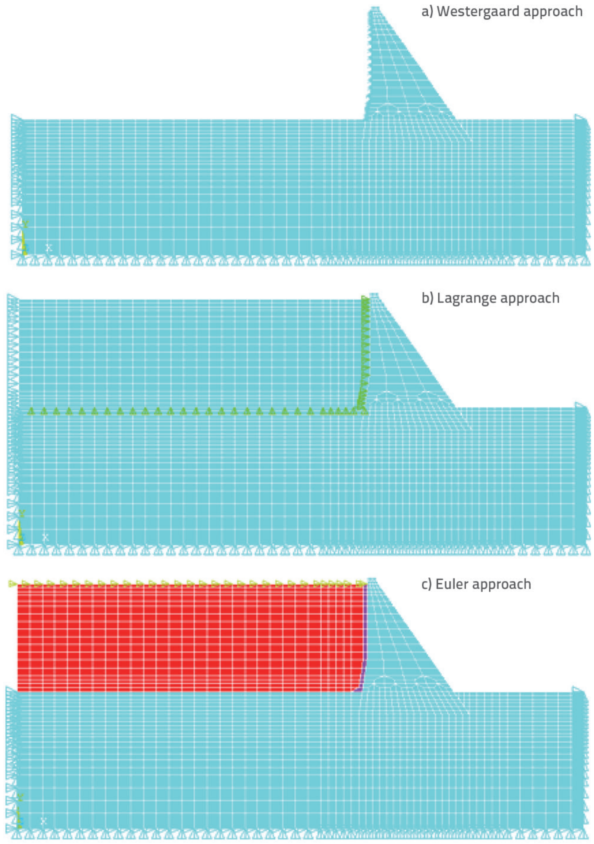

Figure 6. Two-dimensional finite element models of Sarıyar concrete gravity dam including dam-reservoir-foundation systems using Westergaard, Lagrange, and Euler approaches

In these models, the dam body and foundation are represented by solid elements. The reservoir effect is represented by the added masses on the dam body for the Westergaard approach; whereas, in the Lagrange and Euler approaches, the fluid elements define the reservoir water and its hydrodynamic pressures. The foundation of the analysis was treated as being massless. Detailed information regarding the theoretical explanation of the applied SSI method and its effect on the results can be found in the literature [57,58]. Self-weight was considered in all analyses. A mesh convergence study was performed. Modal analyses were performed for different mesh sizes, and the optimum finite-element model was determined at the beginning of the analyses. The maximum element mesh size was specified as 10, 12, and 10 m for the dam body, foundation, and reservoir, respectively. The finite element model applies Plane182 elements to represent the dam body and foundation. In addition, the MASS21, Fluid79, and Fluid29 (structure absent) elements were selected to represent the reservoir water for the Westergaard, Lagrange and Euler Approaches, respectively.

Modal analyses were performed to determine the natural frequencies and related mode shapes for all FSI approaches. The first 15 natural frequencies were obtained at 3.246 to 40.959, 3.301 to 13.198, and 3.258 to 16.538 Hz, and the Rayleigh damping parameters (constants α and β) were calculated as 1.7464–0.00071, 1.4017–0.00156, and 1.3793–0.00178 for the Westergaard, Lagrange, and Euler approaches, respectively, considering the first and tenth mode frequencies. In the dynamic analyses, the element matrices were computed using the Gaussian numerical integration technique. The Newmark method was adopted to solve the equations of motion.

4.1. Displacements

The time histories of the horizontal displacements (upstream-downstream direction) at the crest point obtained from the linear transient analysis under near-fault ground motions with and without pulse signals are presented in Figures 7–8. The maximum attained displacements were 33.73–22.81, 29.33–19.60, and 33.36–24.60 mm for the Westergaard, Lagrange and Euler approaches under pulse and without pulse input motions regarding the 1999 Taiwan Chi-Chi earthquake. Meanwhile, considering the 1979 Imperial Valley earthquake, the maximum attained displacements were 45.10 to 32.61, 37.07 to 30.25, and 47.10 to 30.81 mm corresponding to the three approaches. It can be observed in Figures 7–8 that the pulse ground motions considerably affect the frequency content of the displacements. The displacement increment ratios were calculated as 47.87 %, 49.64 %, and 35.20 % for the 1999 Chi-Chi earthquake and 38.30 %, 22.55 %, and 52.87 % for the 1979 Imperial Valley earthquake, considering the Westergaard, Lagrange, and Euler approaches, respectively.

The variations in the maximum displacements with the dam height for the Westergaard, Lagrange, and Euler approaches are depicted in Figure 9. It can be observed that the displacements increased with the height of the dam body. Minimal displacements were computed using the Lagrange model, while displacements computed using the Westergaard and Euler models show similar values. The maximum differences between

Table 2. Material properties used in the analyses

Material	Material properties		
	Modulus of elasticity [N/m]	Poisson's ratio [-]	Mass per unit volumen [kg/m³]
Dam (concrete)	$35 \cdot 10^9$	0.15	2400
Foundation	$30 \cdot 10^9$	0.2	-
Reservoir	$20.7 \cdot 10^8$	-	1000

all FSI approaches were 15.23 % and 25.32 % for the 1999 Taiwan Chi-Chi earthquake with and without a pulse signal, respectively; these differences were calculated as 27.48 % and 8.19 %, respectively, for the 1979 Imperial Valley earthquake. Moreover, the displacements changed significantly according to the pulse and frequency contents of the ground motion.

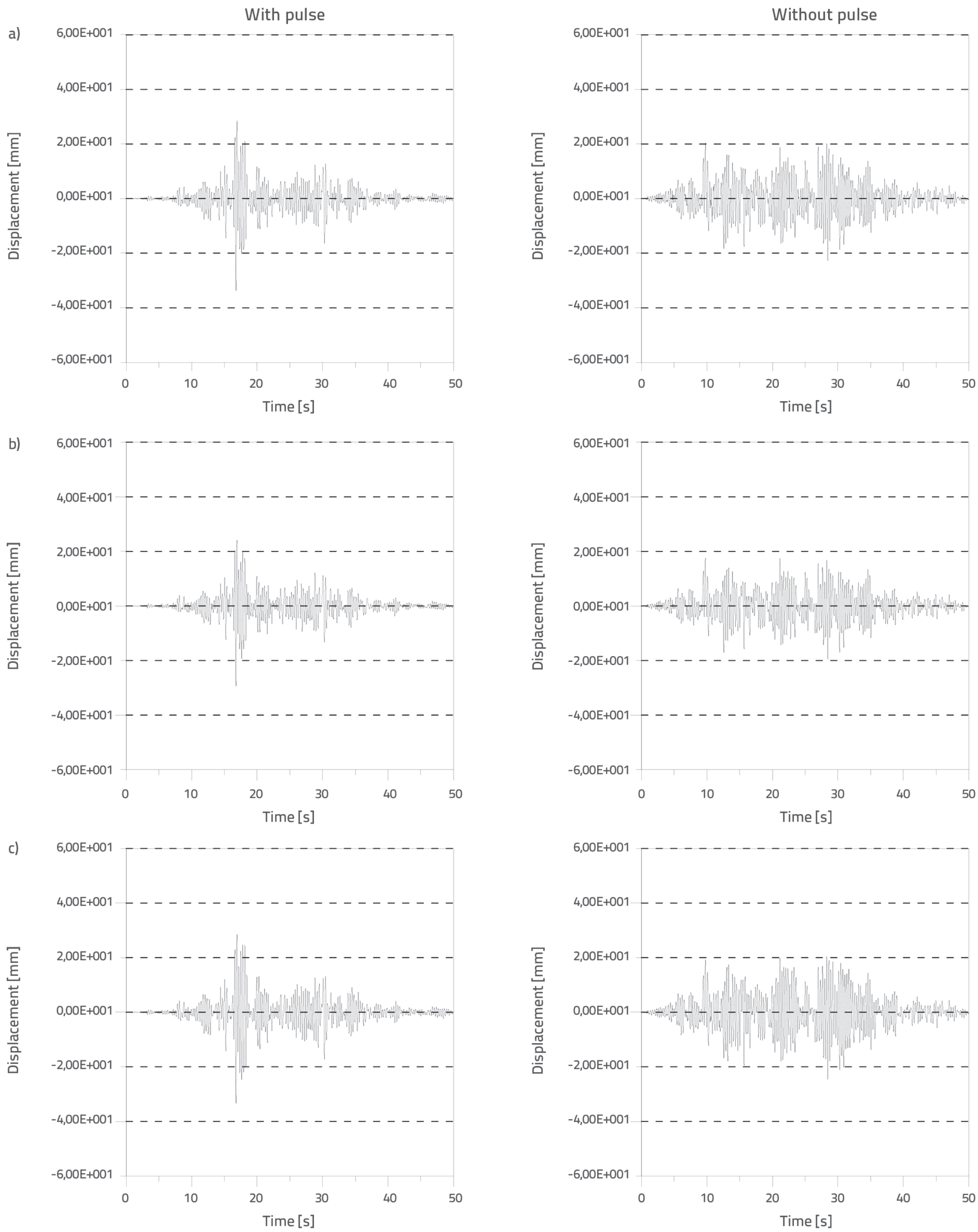

Figure 7. Time histories of horizontal displacements at the crest point considering approaches for 1999 Taiwan Chi-Chi earthquake: a) Westergaard; b) Lagrange; c) Euler

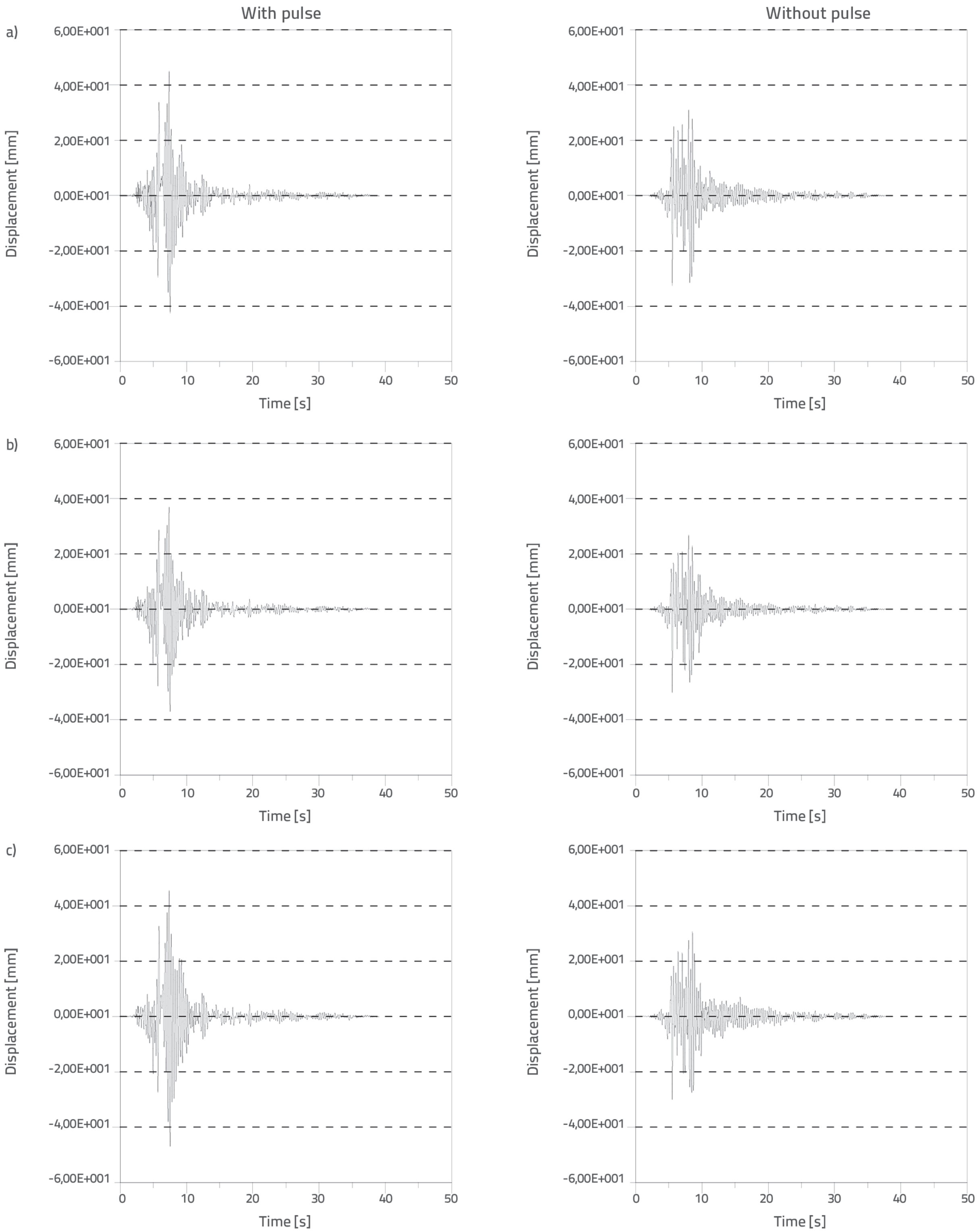

Figure 8. Time histories of horizontal displacements at the crest point considering approaches for 1979 Imperial Valley earthquake: a) Westergaard; b) Lagrange; c) Euler

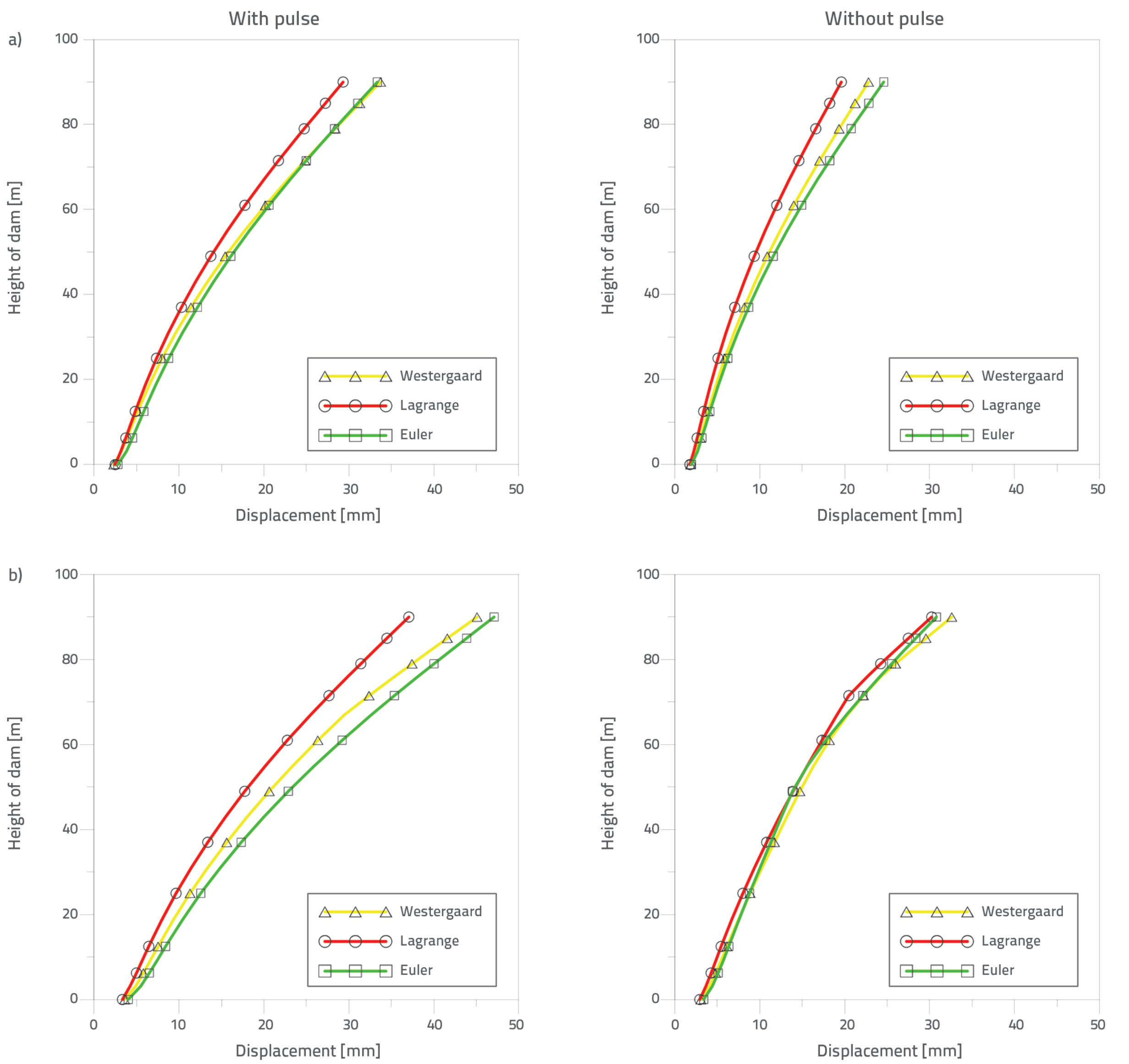

Figure 9. Maximum horizontal displacements by height of Sarıyar concrete gravity dam under: a) 1999 Taiwan Chi-Chi; b) 1979 Imperial Valley earthquakes

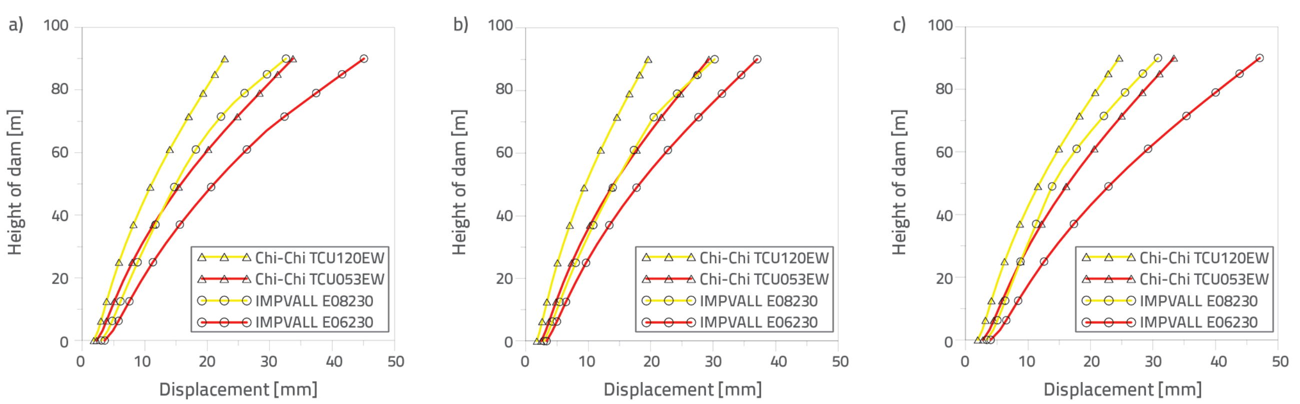

Figure 10. Maximum horizontal displacement by height of Sarıyar concrete gravity dam considering approaches under record motion with pulse (red colour) and without pulse signal (yellow colour): a) Westergaard; b) Lagrange; c) Euler

The variations in the maximum displacements with the height of the dam body for all models in the fluid domain are displayed in Figure 10. As shown in Figures 9 and 10, the dam exhibited horizontal displacement caused by hydrodynamic forces on the bottom of the reservoir. Again, the maximum displacements obtained from near-fault ground motions with a pulse signal were considerably higher than the ground motion without a pulse. In addition, the displacements obtained for the near-fault earthquake records varied according to the FSI approach.

4.2. Principal stresses

The variations in the maximum compressive and tensile principal stresses with height for the Westergaard, Lagrange, and Euler approaches are shown in Figures 11 and 12. It is clear that the maximum values of both principal stresses were attained at 3.1 m from the base of the dam. The maximum tensile stresses were 5.5–4.0, 5.4–4.1, and 5.9–4.3 MPa; whereas, the maximum compressive stresses were 6.6–4.5, 6.7–4.4, and 6.9–4.9 MPa for the Westergaard, Lagrange, and Euler approaches, respectively, considering the 1999 Taiwan Chi-Chi earthquake. In addition, the maximum tensile stresses were determined as 8.5–5.7, 8.6–6.3, and 9.5–5.9 MPa; the maximum compressive stresses were attained as 8.5–6.1, 8.7–6.4, 9.8–6.0 MPa for all FSI approaches considering the 1979 Imperial Valley earthquake. It can be concluded from Figures 11 and 12 that the maximum principal stresses are higher for ground motions with a pulse signal. The stress values attained at 3.125 m were higher for the Euler model, while the peak values were predominantly obtained using the Westergaard model. More specifically, the stress values varied according to the pulse and frequency content of the ground motions. The corresponding diagrams include the self-weight and stresses/strains under hydrodynamic pressure.

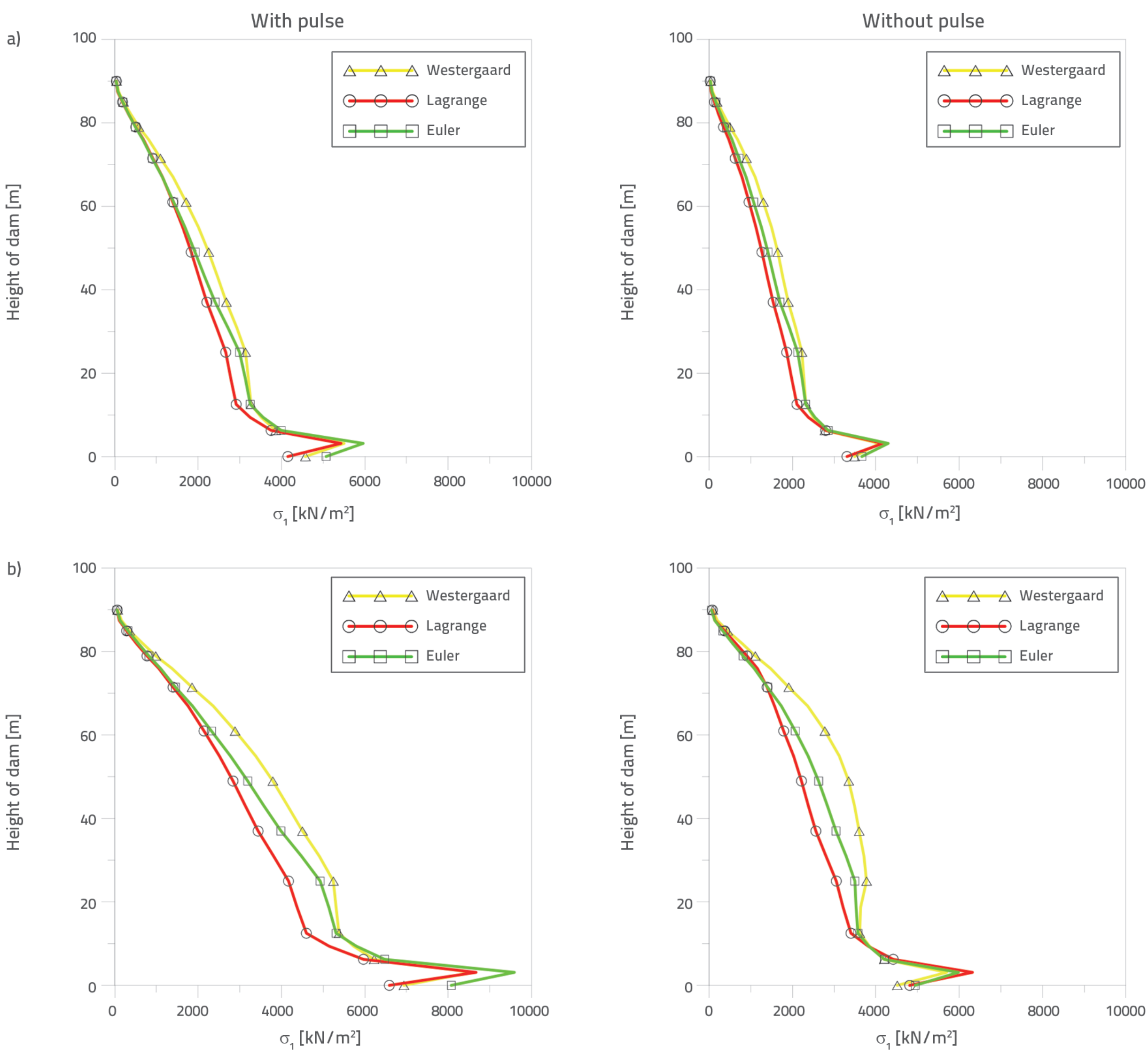

Figure 11. Maximum tensile principal stress with height of Sarıyar concrete gravity dam under: a) 1999 Taiwan Chi-Chi; b) 1979 Imperial Valley earthquakes

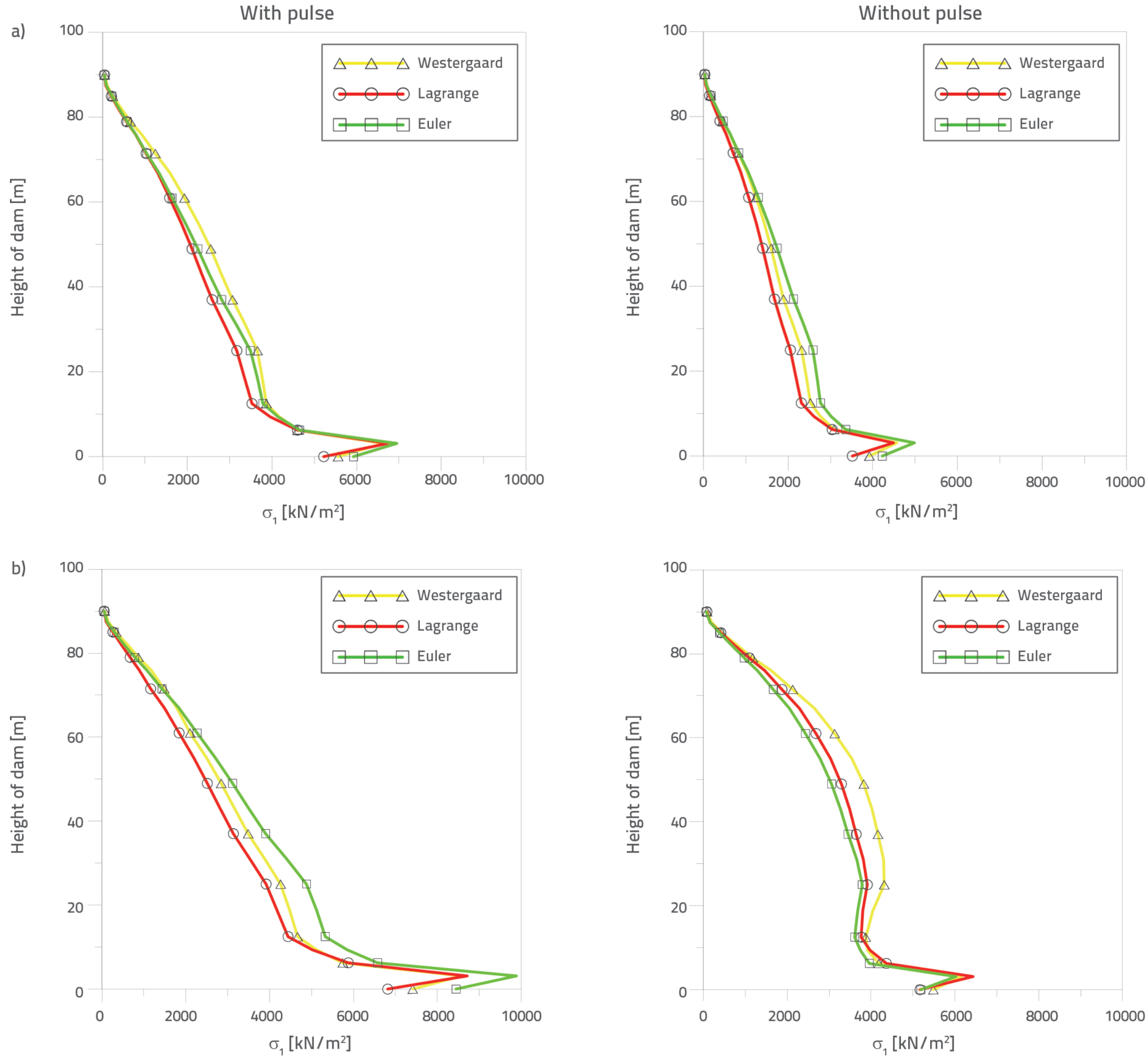

Figure 12. Maximum compressive principal stresses with height of Sarıyar concrete gravity dam under: a) 1999 Taiwan Chi-Chi; b) 1979 Imperial Valley earthquakes

The variations in the maximal and minimal principal stresses with height for all models of the fluid domain are shown in Figures 13 to 14. It is apparent that the stress magnitude decreases along the dam height, where the maximum stresses obtained in the case of near-fault ground motion with a pulse signal are higher than those obtained under ground motions without a pulse. In addition, the stresses varied according to the FSI approach. Peak stress values obtained near the dam crest were higher for recorded motions without a pulse signal.

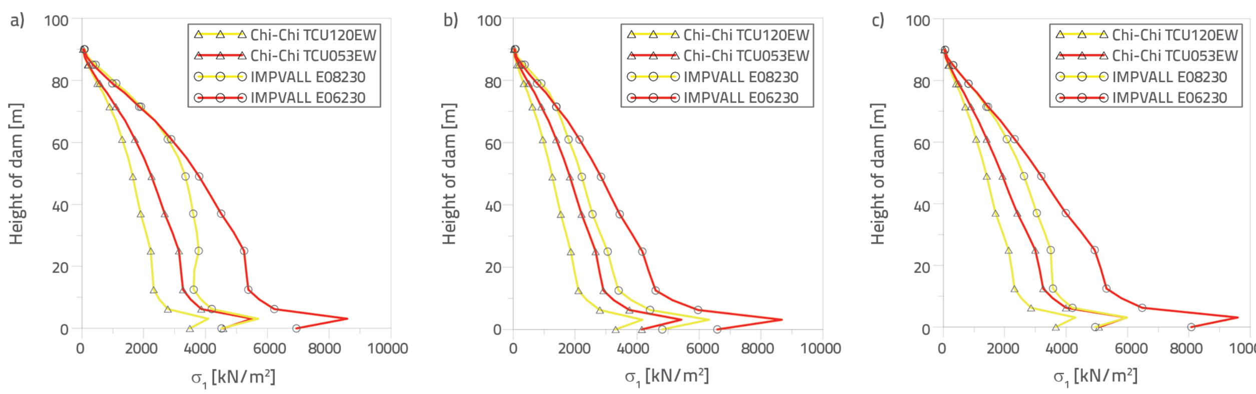

Figure 13. Maximum tensile stress with height considering approaches for ground motions with (red colour) and without pulse signal (yellow colour): a) Westergaard; b) Lagrange; c) Euler

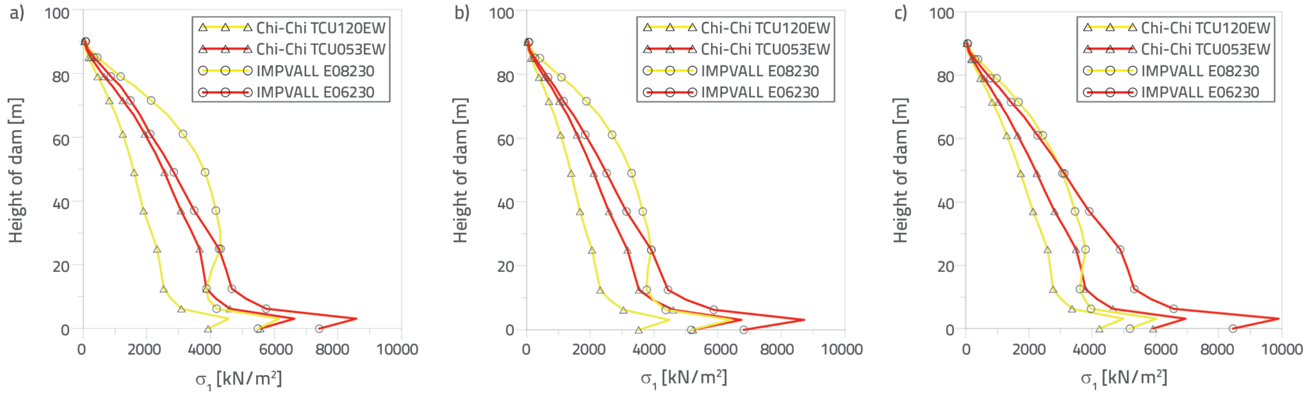

Figure 14. Maximum compressive stress with height from approaches for ground motions with (red colour) and without pulse signal (yellow colour): a) Westergaard; b) Lagrange; c) Euler

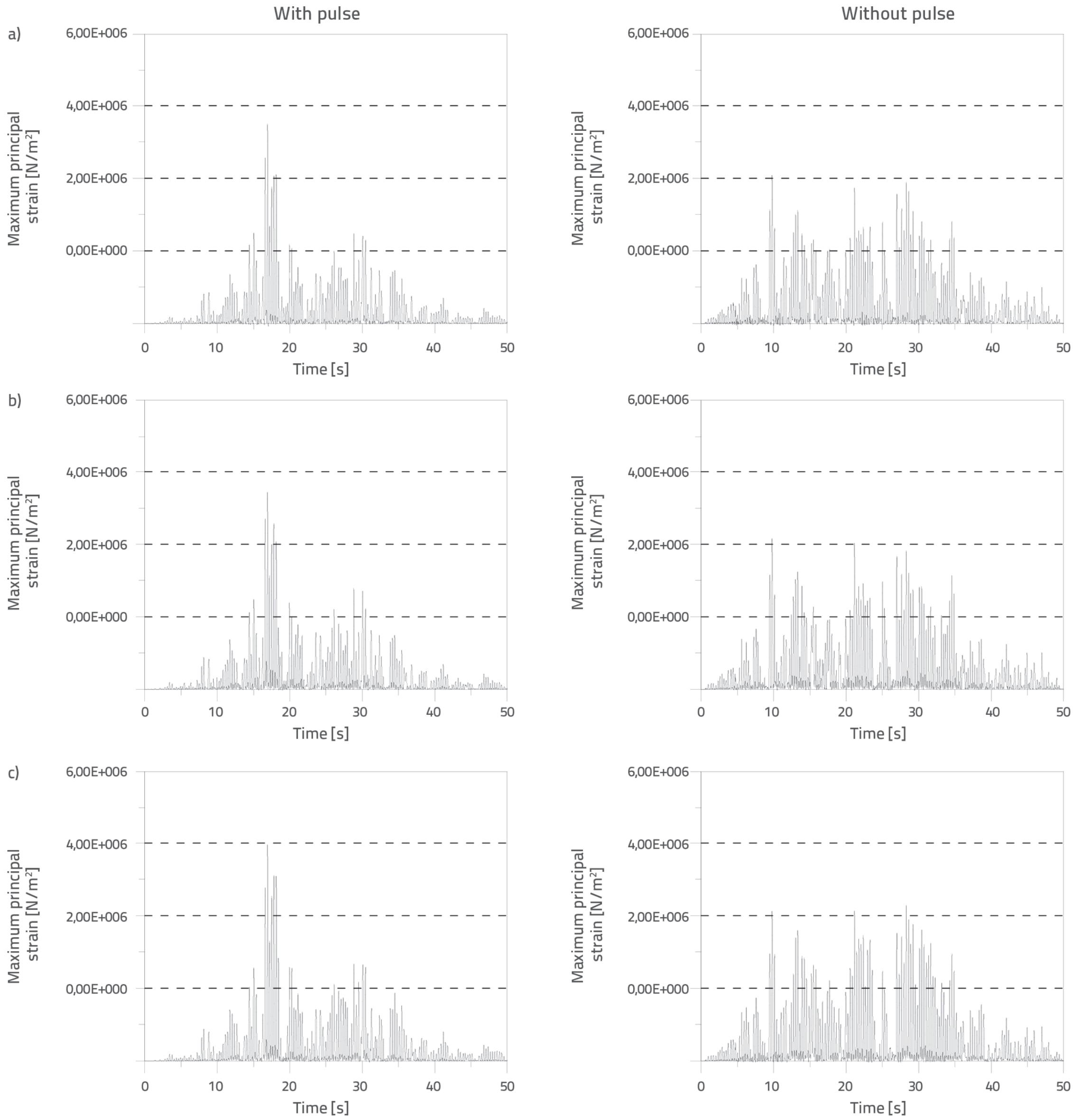

Figure 15. Time histories of maximum principal stress at node close to the bottom from approaches under the 1999 Taiwan Chi-Chi earthquake: a) Westergaard; b) Lagrange; c) Euler

The time histories of the maximum and minimum principal stresses (3.125 m above the base point of the dam-foundation interaction node at the upstream face) are presented in Figures 15–18. For the other response parameters, the maximum principal stresses were higher for ground motions with a pulse signal. Although the stress values attained at 3.125 m were the highest for the Euler models overall, the peak value was obtained with the Lagrange model under the 1979 Imperial Valley earthquake record without pulses.

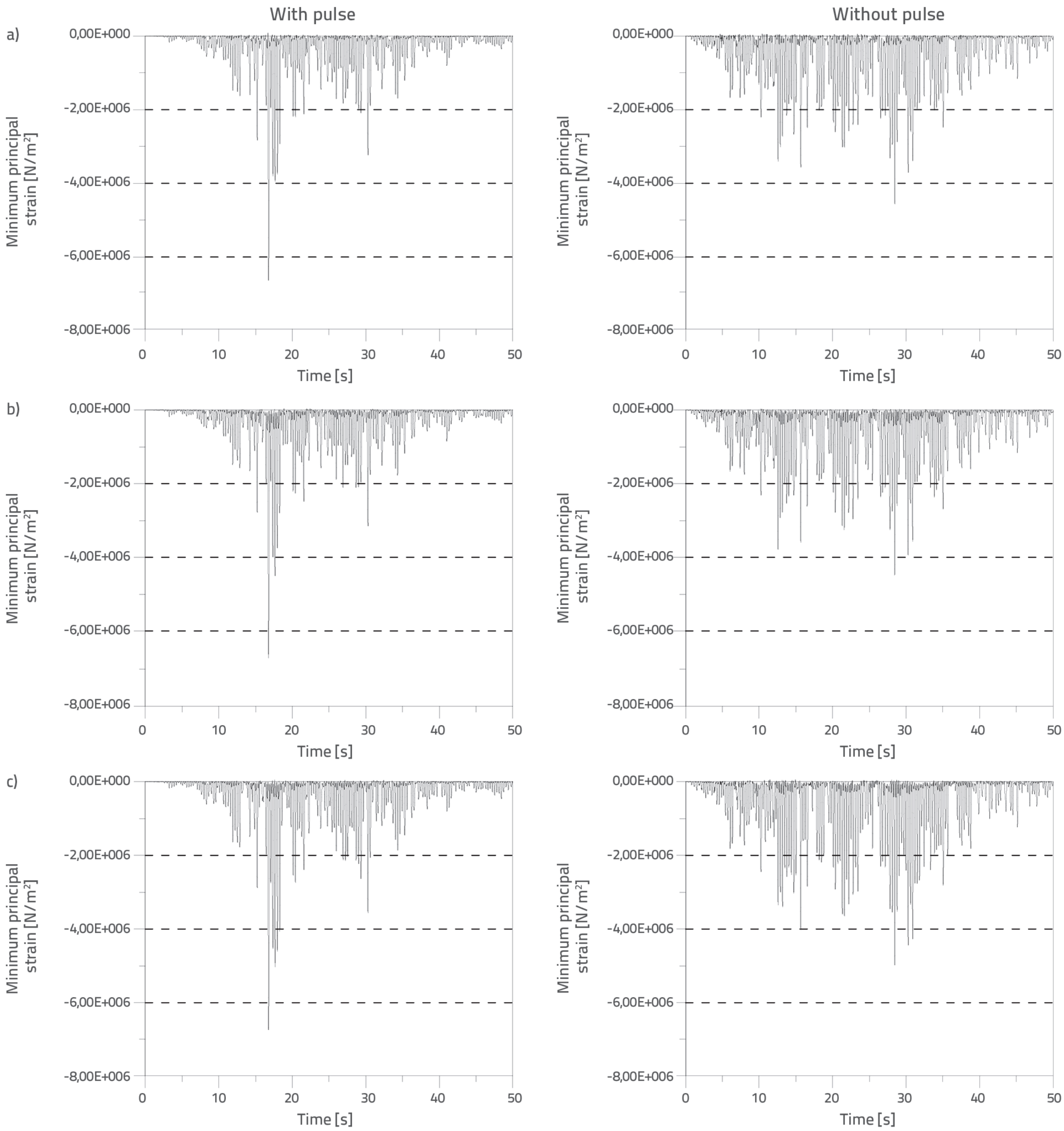

Figure 16 .Time histories of minimum principal stress at node close to the bottom from approaches under the 1999 Taiwan Chi-Chi earthquake: a) Westergaard; b) Lagrange; c) Euler

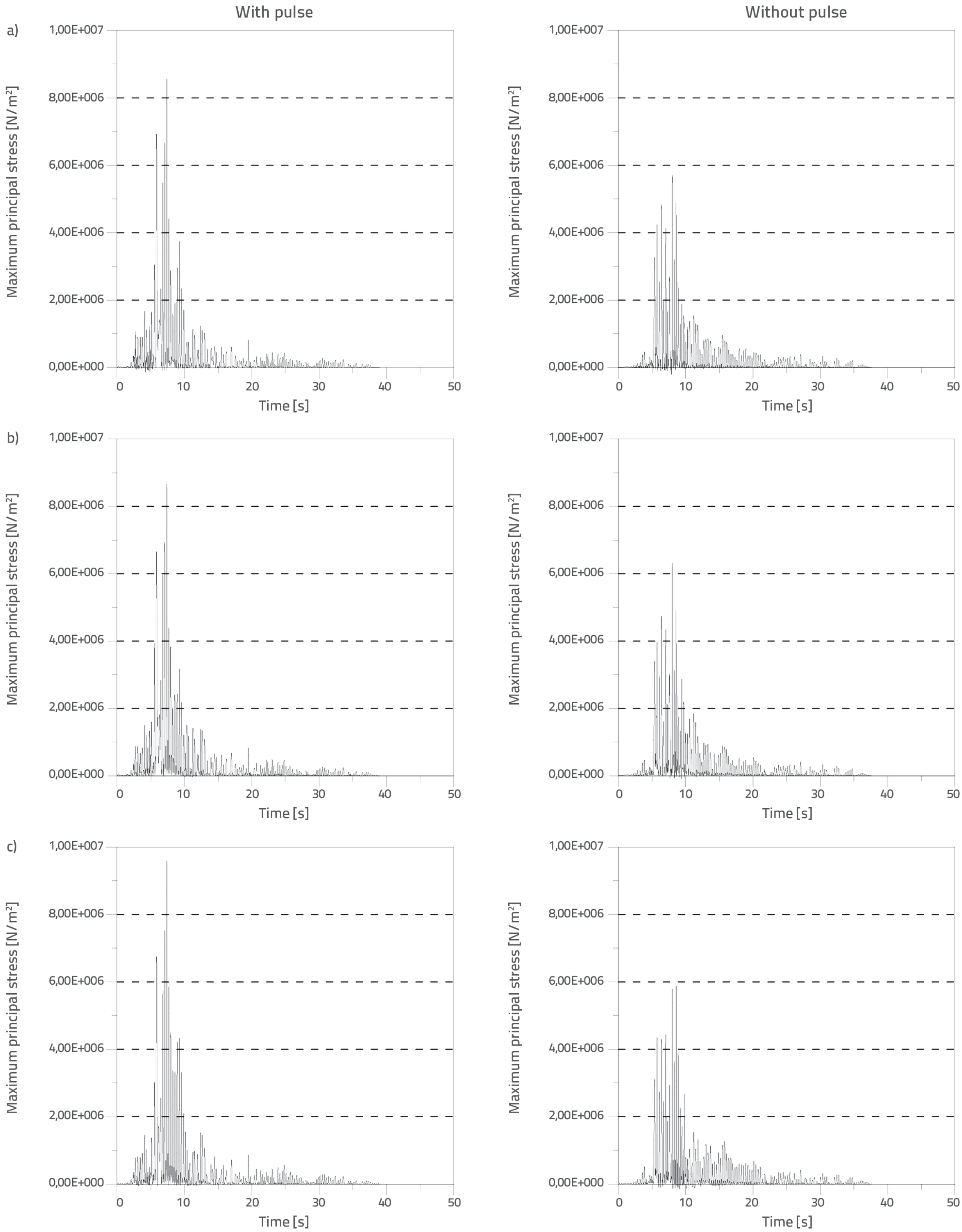

Figure 17. Time histories of maximum principal stress at node close to the bottom consideringapproaches under the 1979 Imperial Valley earthquake: a) Westergaard; b) Lagrange; c) Euler

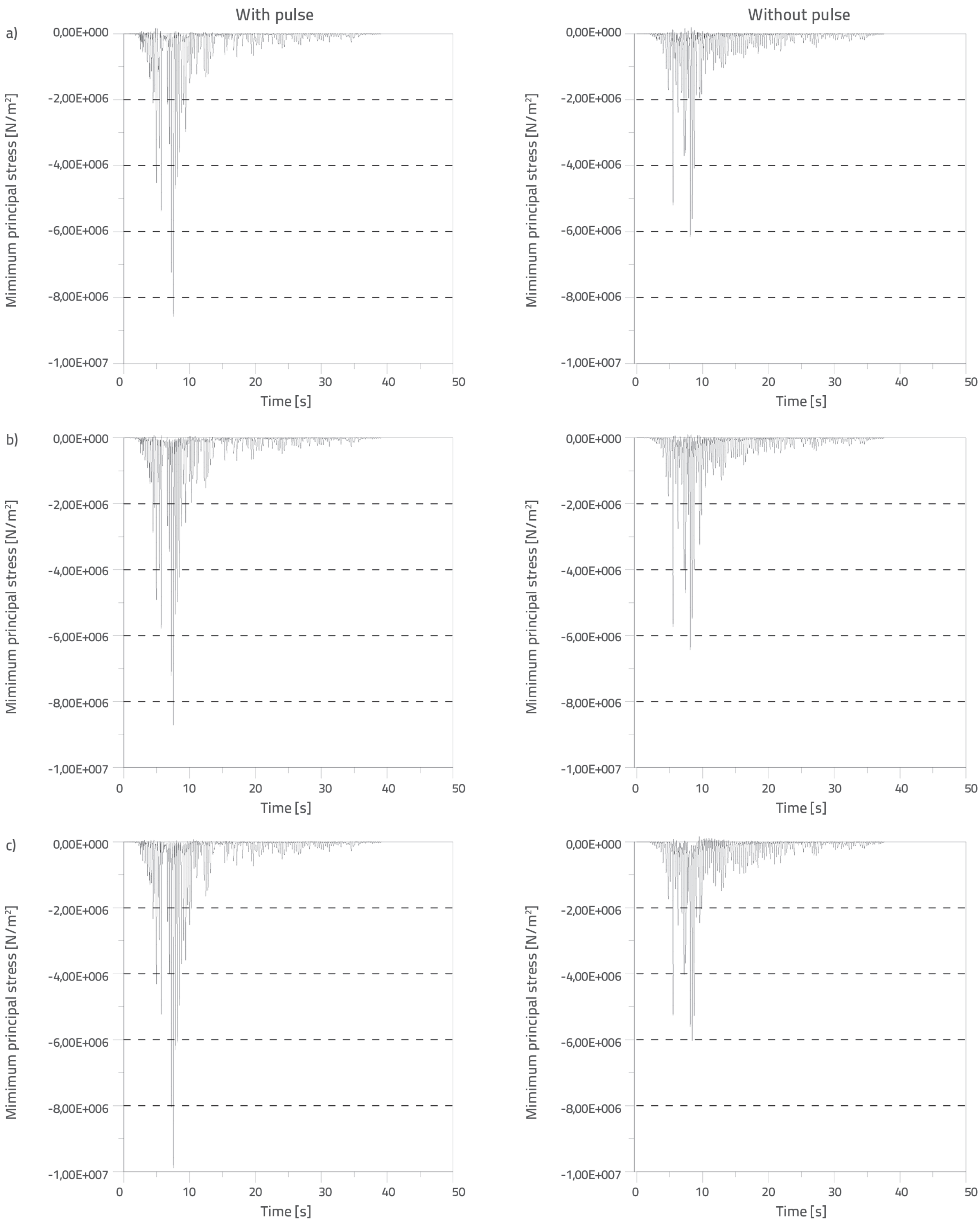

Figure 18.Time histories of minimum principal stress at node close to the bottom considering approaches under the 1979 Imperial Valley earthquake: a) Westergaard; b) Lagrange; c) Euler

4.3. Principal Strains

The variations in the maximum compressive and tensile principal strains with height calculated from the Westergaard, Lagrange, and Euler approaches are depicted in Figures 19–20. The figures clearly show that the maximum values of both principal strains were attained at 3.1 m from the base of the dam. The maximum tensile strains were (15,5 · 10^{-5}) - (11,5 · 10^{-5}), (15,4 · 10^{-5}) - (11,8 · 10^{-5}), (16,9 · 10^{-5}) - (12,2 · 10^{-5}); whereas, the maximum compressive strains were (18,7 · 10^{-5}) - (12,9 · 10^{-5}), (19,2 · 10^{-5}) - (12,7 · 10^{-5}), (19,7 · 10^{-5}) - (14,1 · 10^{-5}) from the Westergaard, Lagrange, and Euler approaches, respectively, for the 1999 Taiwan Chi-Chi earthquake. In addition, the maximum tensile strains were (24,1 · 10^{-5}) - (16,0 · 10^{-5}), (24,7 · 10^{-5}) - (17,9 · 10^{-5}), (27,2 · 10^{-5}) - (16,8 · 10^{-5}); the maximum compressive strains were (24,2 · 10^{-5}) - (17,4 · 10^{-5}), (24,8 · 10^{-5}) - (18,2 · 10^{-5}), (28,0 · 10^{-5}) - (17,1 · 10^{-5}) from all FSI approaches considering the 1979 Imperial Valley earthquake. It can be concluded from Figures 19 and 20 that the maximum principal strains were higher for ground motions with a pulse signal. The strain values attained at 3.125 m were higher for the Euler model, but the peak values were obtained using the Westergaard model. In addition, the strain values obtained from all models of the fluid domain varied according to the pulse and frequency content of the ground motion.

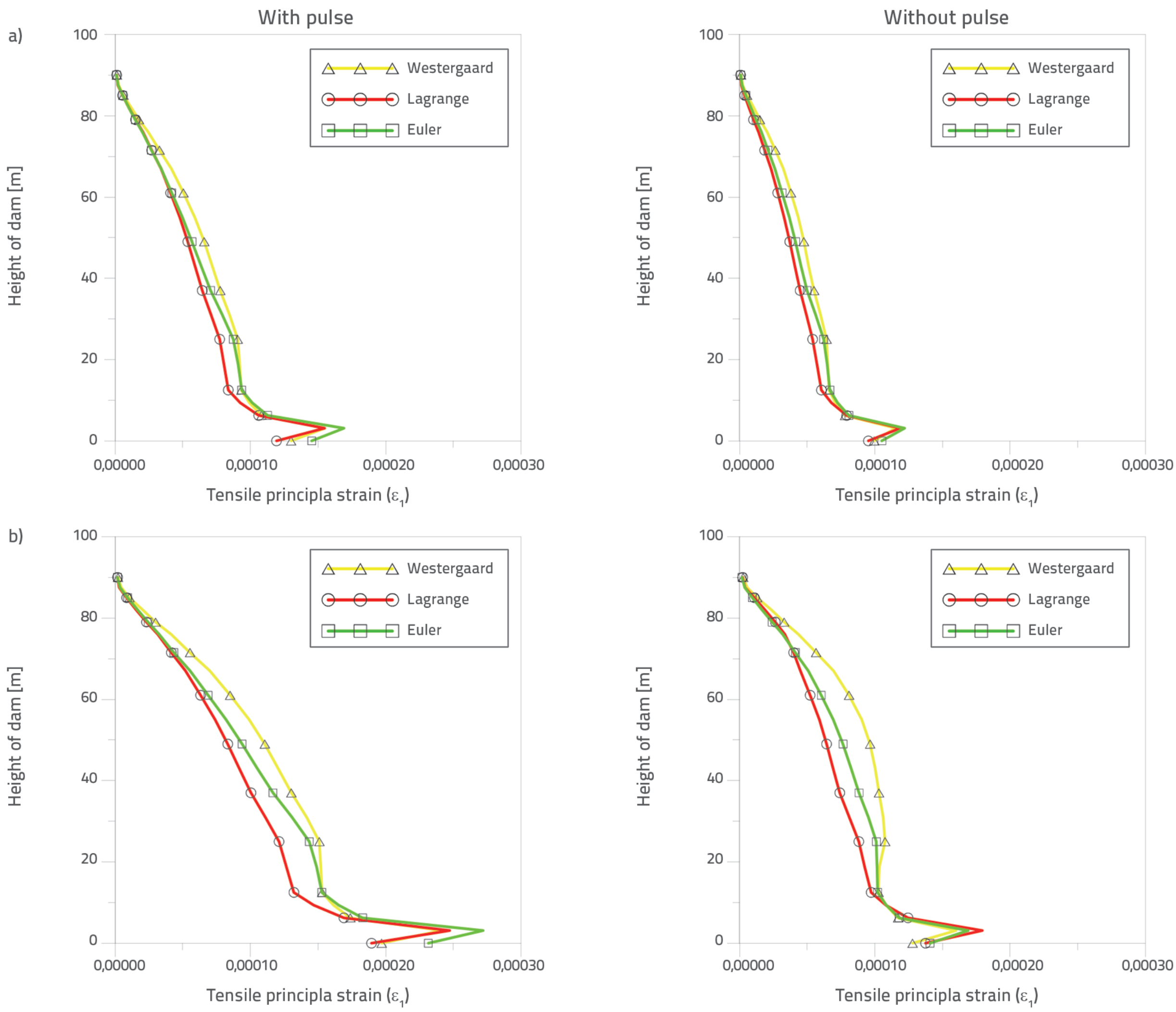

Figure 19. Maximum tensile principal strain with height of Sarıyar concrete gravity dam under: a) 1999 Taiwan Chi-Chi; b) 1979 Imperial Valley earthquakes

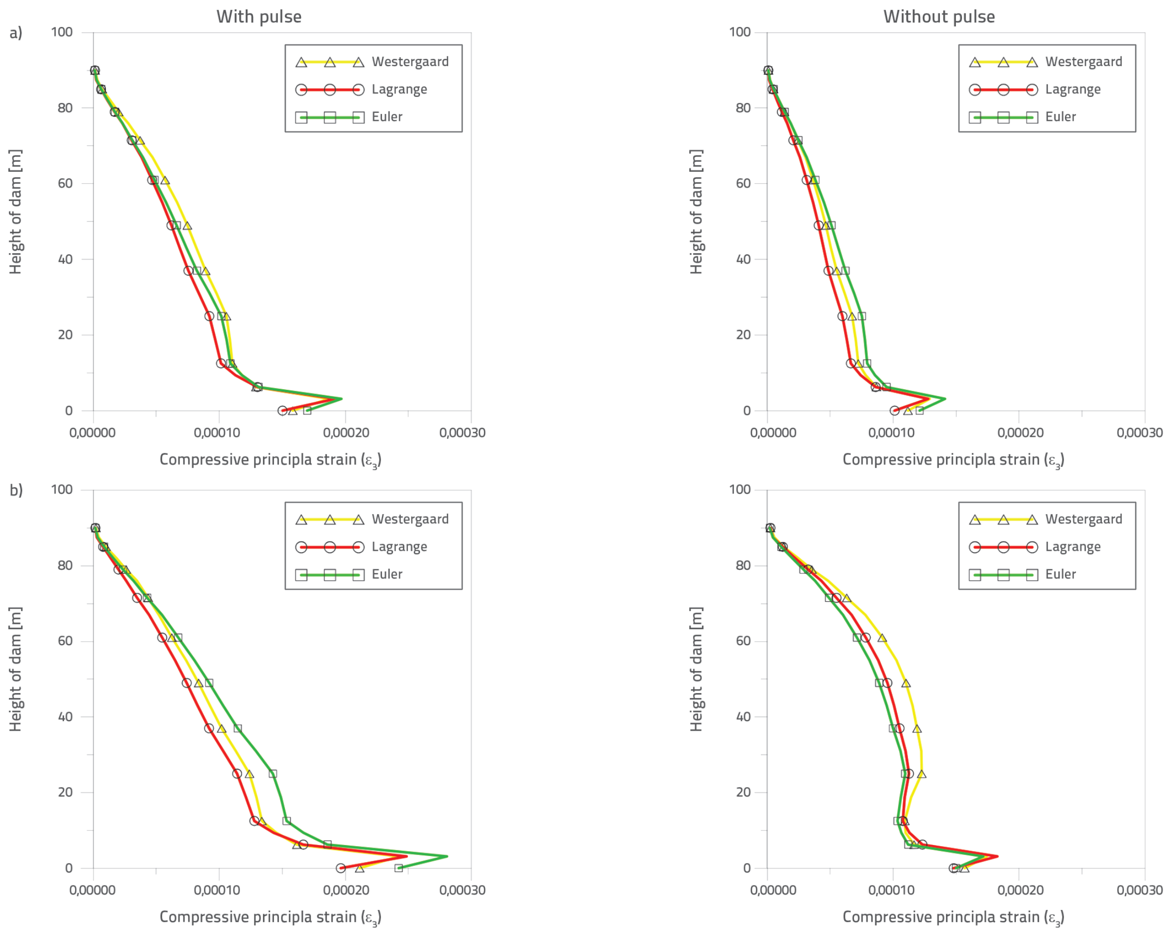

Figure 20. Maximum compressive principal strain with height of Sarıyar concrete gravity dam under: a) 1999 Taiwan Chi-Chi; b) 1979 Imperial Valley earthquakes

The variations in the maximal and minimal principal strains with height for all models of the fluid domain are presented in Figures 21 and 22. It is apparent that the strain magnitude decreases along the dam height, while the maximum strain obtained in the case of near-fault ground motion with a pulse signal is higher than that obtained under ground motions without a pulse. In addition, the strains varied according to the FSI approach. Peak strain values obtained near the dam crest were higher for recorded motions without a pulse signal.

The time histories of the maximum and minimum principal stresses (3.125 m above the base point of the dam-foundation interaction node at the upstream face) are displayed in Figures 23 to 26. For the other response parameters, the maximum principal strains were higher for ground motions with a pulse signal. Although the strain values attained at 3.125 m were the highest from the Euler model overall, the peak value was obtained with the Lagrange model under the 1979 Imperial Valley earthquake record without pulses.

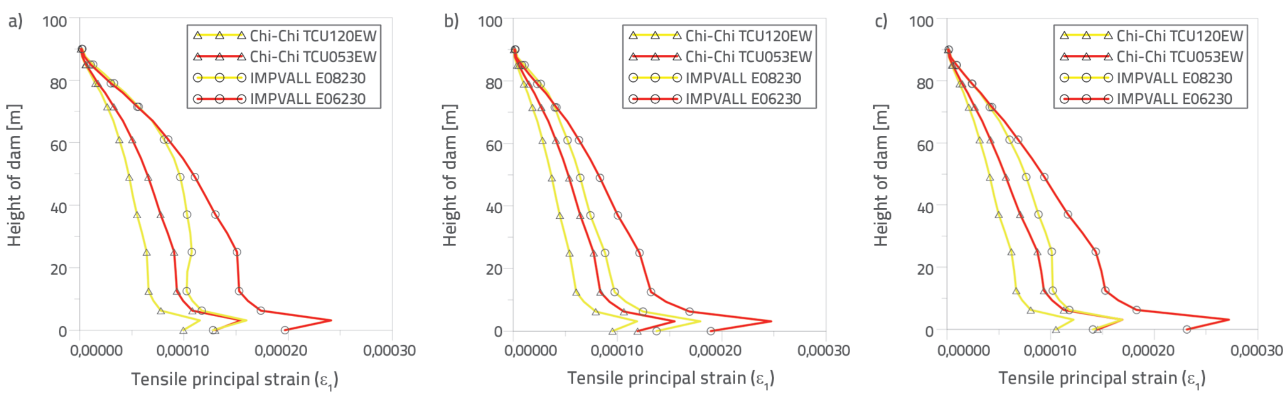

Figure 21. Maximum tensile strain with height considering approaches for ground motions with (yellow colour) and without pulse signal (red colour): a) Westergaard; b) Lagrange; c) Euler

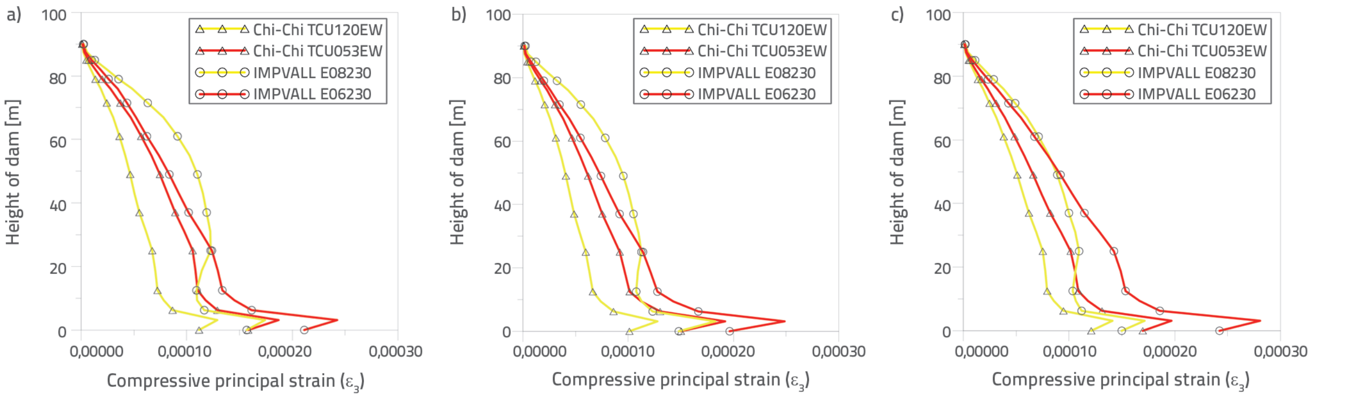

Figure 22. Maximum compressive strain with height from approaches for ground motions with and without pulse signal: a) Westergaard; b) Lagrange; c) Euler

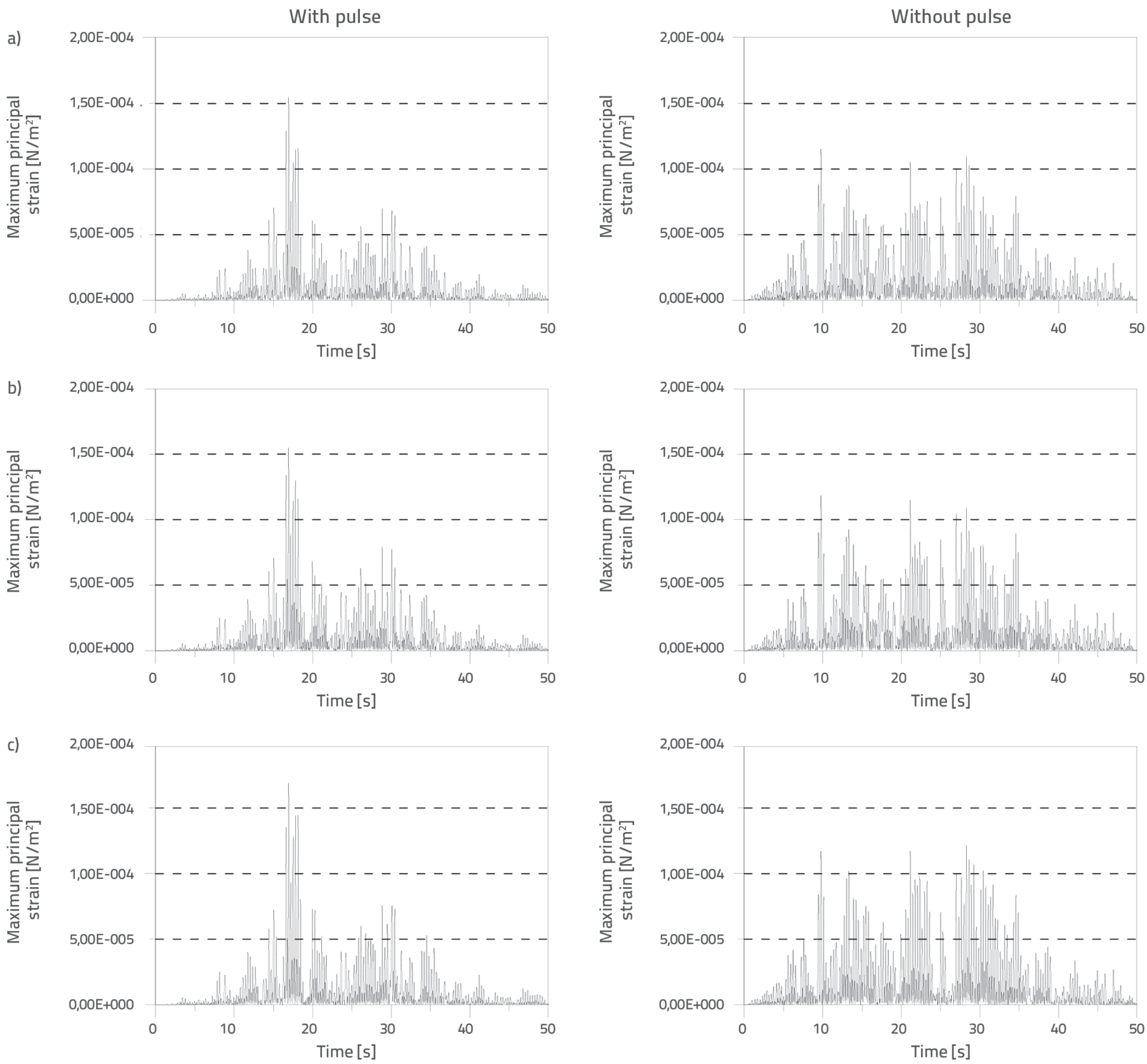

Figure 23 Time histories of maximum principal strain at crest point from approaches for the 1999 Taiwan Chi-Chi earthquake: a) Westergaard; b) Lagrange; c) Euler

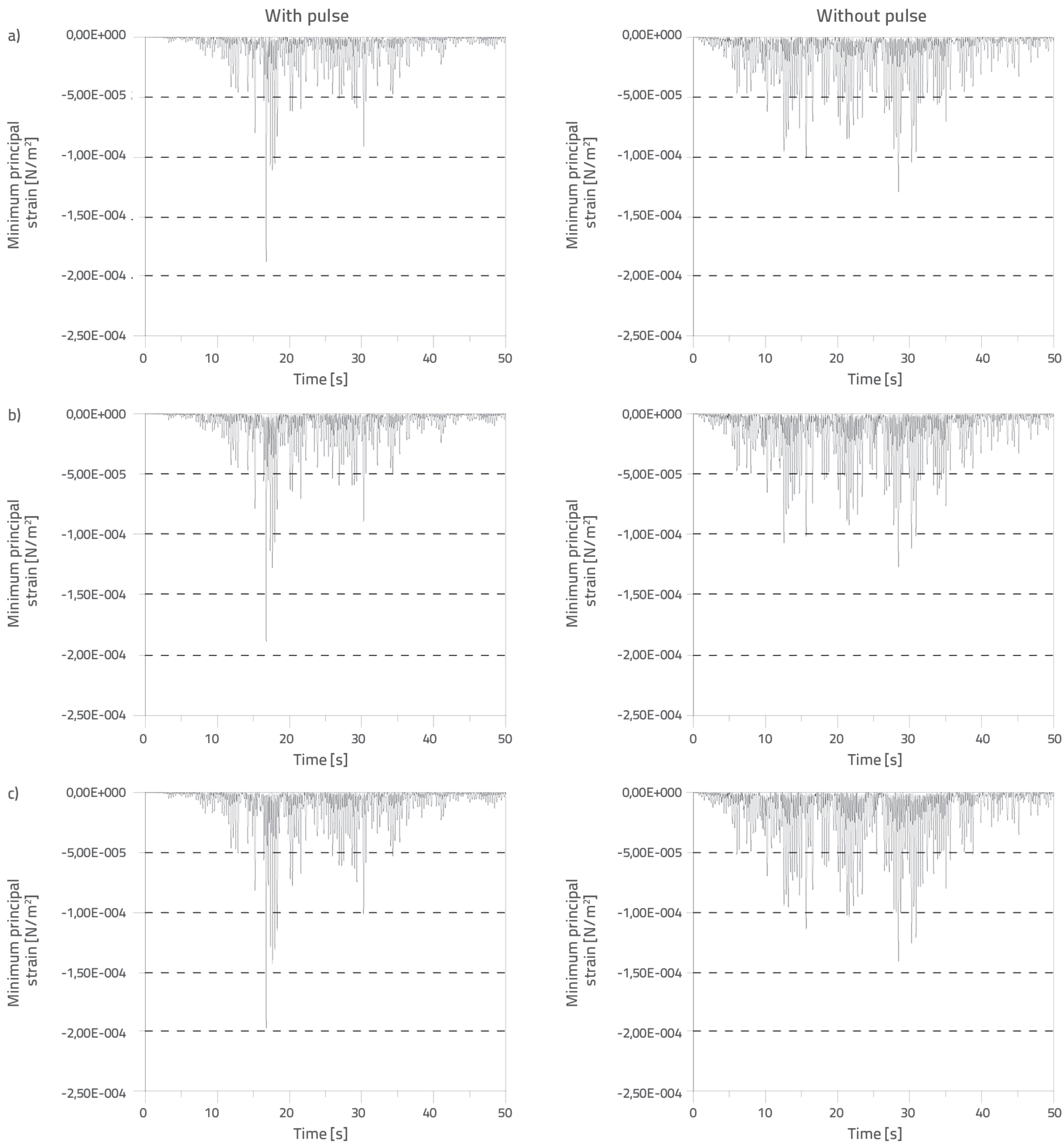

Figure 24. Time histories of minimum principal strain at crest point from approaches for the 1999 Taiwan Chi-Chi earthquake: a) Westergaard; b) Lagrange; c) Euler

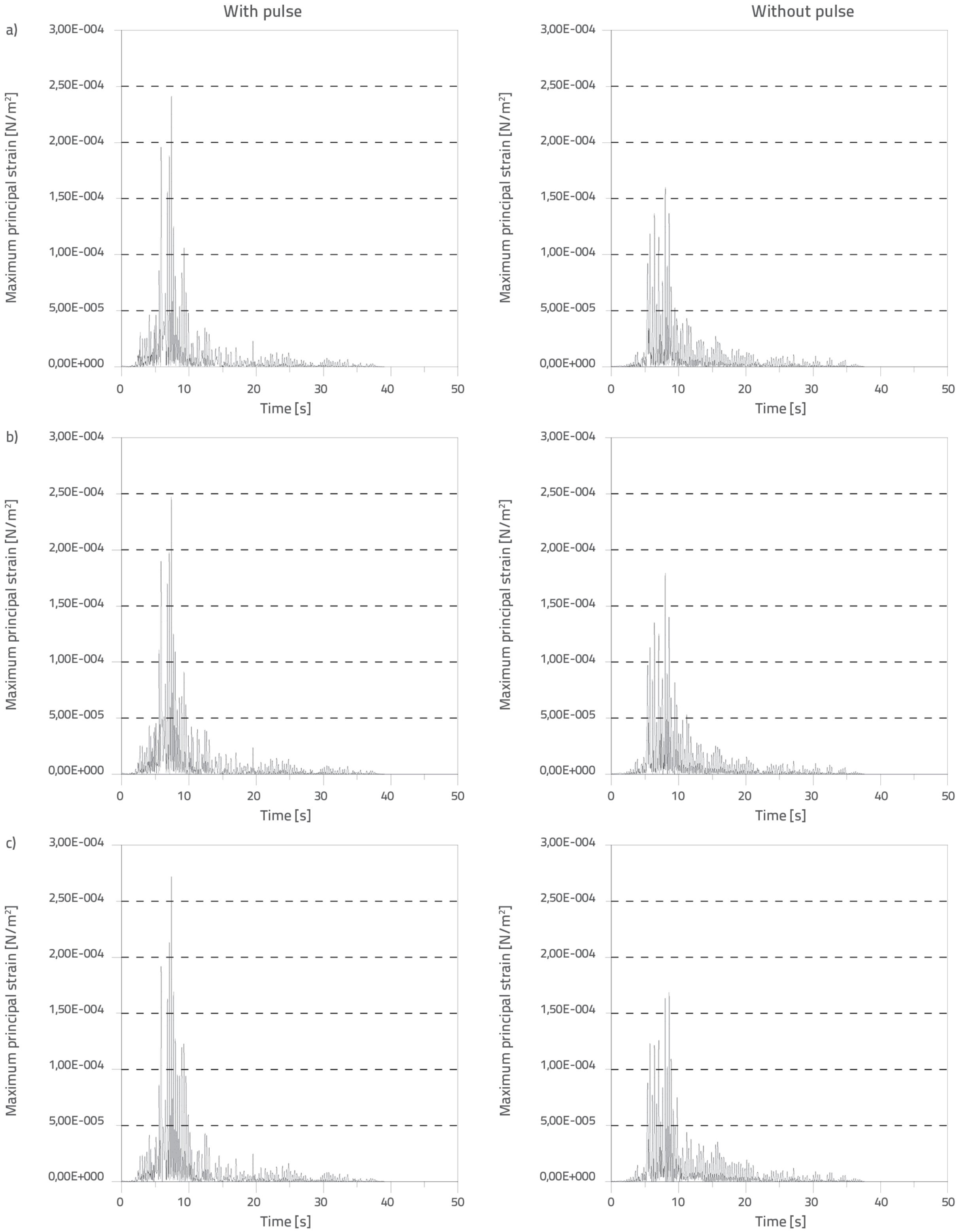

Figure 25. Time histories of maximum principal strain at crest point from approaches for the 1979 Imperial Valley earthquake: a) Westergaard; b) Lagrange; c) Euler

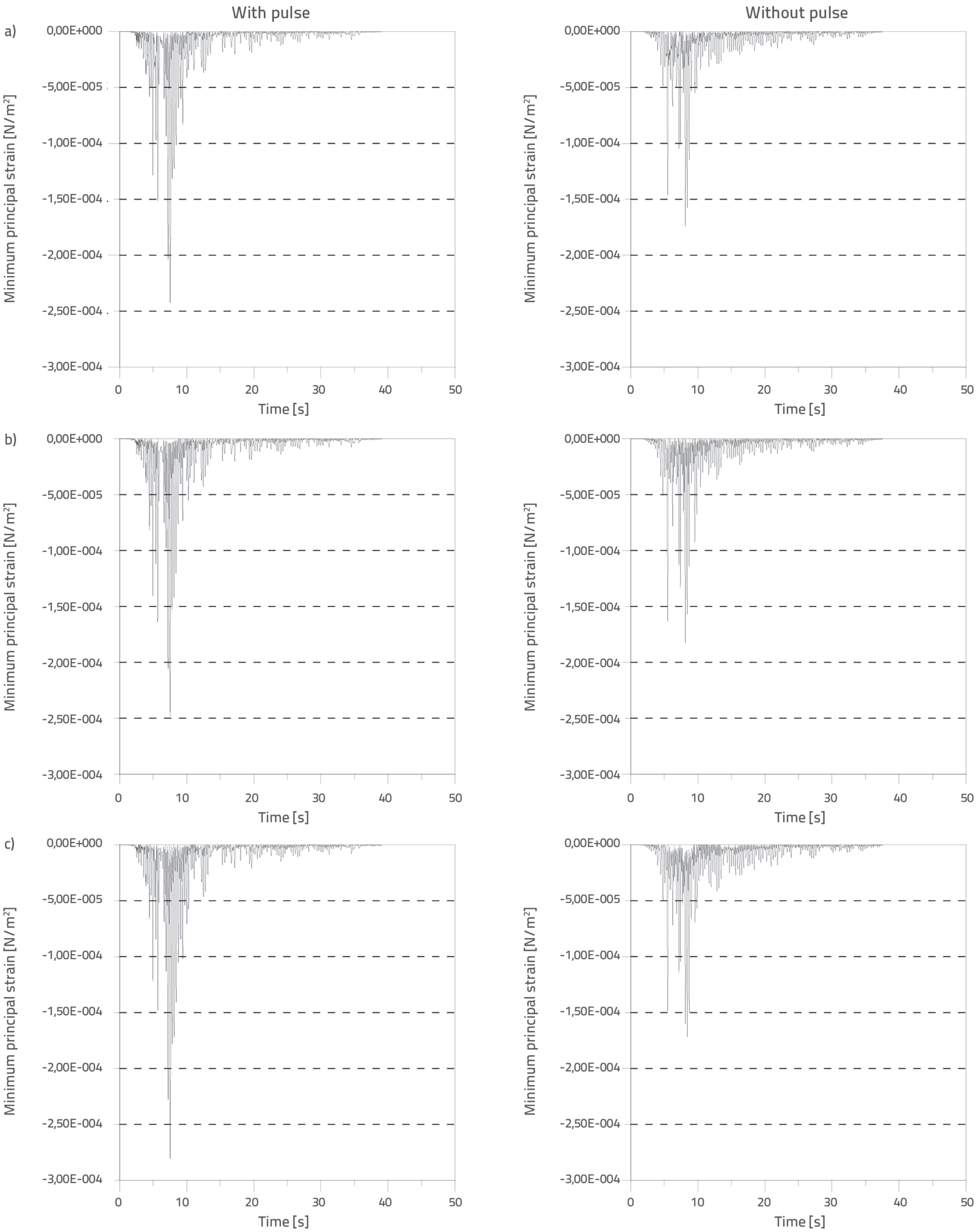

Figure 26. Time histories of minimum principal strain at crest point considering approaches for the 1979 Imperial Valley earthquake: a) Westergaard; b) Lagrange; c) Euler

5. Conclusions

The effects of near-fault ground motions with pulse signals on the structural dynamic response of concrete gravity dams, including the dam-reservoir-foundation interaction, were presented. Different FSI approaches of Westergaard (added masses), Lagrange (displacement-based), and Euler (pressure-based) for assessment of the hydrodynamic pressure were applied. The Sarıyar concrete gravity dam, located in Ankara, Turkey, was selected as a case study. The near-fault records of the 1999 Taiwan Chi-Chi and 1979 Imperial Valley earthquakes were considered representative of ground motion with and without pulse signals, respectively.

The completed analyses show that the displacement increases with height of the dam for all ground motions and modelling approaches. The maximum tensile and compressive stresses and strains were obtained at the height of 3.125 m from the dam base. The maximum and minimum principal stresses and strains showed a decreasing trend from the bottom (3.125 m from the base of the dam) to the top of the dam crest. Although the ground motions with and without the pulse signal had the same peak ground acceleration, the maximum values were obtained from near-fault ground motions with a pulse.

The displacements obtained from the pulse input motions were considerably higher than those obtained without the pulse input motions. The displacement increment ratios were calculated as 47.87 %, 49.64 %, and 35.20 % for the 1999 Chi-Chi earthquake and 38.30 %, 22.55 %, and 52.87 % for the 1979 Imperial Valley earthquake, considering the Westergaard, Lagrange, and Euler approaches, respectively.

The maximum and minimum principal stresses obtained from the pulse input motions were considerably higher than those obtained without pulse input motions. The tensile stress values show an increasing trend with the pulse signals. The maximum differences were 37.50 %, 31.70 %, and 37.21 % for the 1999 Chi-Chi earthquake and 49.12 %, 36.51 %, and 61.02 % for the Imperial Valley earthquake, considering the Westergaard, Lagrange, and Euler approaches, respectively. These increment ratios were calculated for the minimum compressive stress as 46.67 %, 52.27 %, and 40.82 % for the 1999 Chi-Chi earthquake and 39.34 %, 35.94 %, and 63.33 % for the Imperial Valley earthquake, respectively.

The strain values obtained with the pulse signal were higher than those obtained without pulse signals. The maximum differences in tensile strains were determined as 34.78 %, 30.51 %, and 38.52 % for the 1999 Chi-Chi earthquake and 50.63 %, 37.99 %, and 61.90 % for the Imperial Valley earthquake, considering the Westergaard, Lagrange, and Euler approaches, respectively. In addition, the maximum differences in compressive strains were determined as 44.96 %, 51.18 %, 39.72 %, 39.08 %, 36.26 %, and 63.74 % for both earthquakes, considering all approaches.

The displacement, stress, and strain values obtained from all models of the fluid domain vary with respect to the pulse occurrence and frequency content of the ground motion.

The MASS21 element, coupling lines, and FLUID29 element (using structure present options) can be considered as the dam-reservoir and reservoir-foundation interactions in the Westergaard, Lagrange, and Euler approaches, respectively.

It can be concluded that for the same peak ground acceleration and duration of near-fault ground motions, that with a pulse signal generates considerably higher displacements, stresses, and strains in concrete gravity dams. Near-fault ground motions with pulse signals have a remarkable effect on the structural performance of concrete gravity dams and should be considered to obtain more realistic results for concrete gravity dams in seismic-prone areas.

REFERENCES

[1] Westergaard, H.M.: Water Pressures on Dams during Earthquakes, Transactions of the American Society of Civil Engineers, 98 (1933) 2, pp. 418–433

[2] Calayır, Y.: Dynamic Analysis of Concrete Gravity Dams Using Euler and Lagrange Approaches, PhD. Thesis, Karadeniz Technical University, Trabzon, Turkey, 1994.

[3] Calayır, Y., Dumanoğlu, A.A., Bayraktar, A.: Earthquake analysis of gravity dam–reservoir systems using the Eulerian and Lagrangian approaches, Computers and Structures, 59 (1996) 5, pp. 877–890

[4] Bayraktar, A., Altunışık, A.C., Sevim, B., Kartal, M.E., Türker, T.: Near-fault ground motion effects on the nonlinear response of the dam-reservoir-foundation systems, Structural Engineering & Mechanics, 28(2008) 4, pp. 411-442

[5] Bayraktar, A., Altunișik, A.C., Sevim, B., Kartal, M.E, Türker, T., Bilici, Y.: Comparison of near- and far-fault ground motion effect on the nonlinear response of dam-reservoir-foundation systems, Nonlinear Dynamics, 58 (2009) 4, pp.655-673

[6] Bayraktar, A., Türker, T., Akköse, M., Ateș, Ș.: The effect of reservoir length on seismic performance of gravity dams to near- and far-fault ground motions, Natural Hazards, 52 (2010) 2, pp. 257-275

[7] Zhang, S., Wang, G.: Effects of near-fault and far-fault ground motions on nonlinear dynamic response and seismic damage of concrete gravity dams, Soil Dynamics and Earthquake Engineering, 53 (2013), pp. 217-229

[8] Maity, D., Bhattacharyya, S.K.: A parametric study fluid-structure interaction problems, Journal of Sound and Vibration, 263 (2003) 4, pp. 917-935

[9] Samii, A., Lotfi, V.: Comparison of coupled and decoupled modal approaches in seismic analysis of concrete gravity dams in time domain, Finite Elements in Analysis and Design, 43 (2007), pp. 1003-1012

[10] Fathi, A., Lotfi, V.: Effects of reservoir length on dynamic analysis of concrete gravity dams, Proceedings of the 14th World Conference on Earthquake Engineering, Beijing, China, 2008.

[11] Akköse, M., Șimșek, E.: Non-linear seismic response of concrete gravity dams to near-fault ground motions including dam-water-sediment-foundation interaction, Applied Mathematical Modelling, 34 (2010), pp. 3685–3700

[12] Wood, C., Gil, A.J., Hassan, O., Bonet, J.: Partitioned block-Gauss–Seidel coupling for dynamic fluid–structure interaction, Computers and Structures, 88 (2010) 23-24, pp. 1367-1382

[13] Gogoi, I., Maity, D.: A novel procedure for determination of hydrodynamic pressure along upstream face of dams due to earthquakes, Computers and Structures, 88 (2010) 5-6, pp. 539-548

[14] Degroote, J., Annerel, S., Vierendeels, J.: Stability analysis of Gauss–Seidel iterations in a partitioned Simulation of fluid–structure interaction, Computers and Structures, 88 (2010) 5-6, pp. 263-271

[15] Sevim, B., Altunişik, A.C., Bayraktar, A., Akköse, M. and Calayir, Y.: Water length and height effects on the earthquake behavior of arch dam-reservoir-foundation systems, KSCE Journal of Civil Engineering, 15 (2011) 2, pp. 295-303

[16] Heydari, M.M., Mansoori, A.: Dynamic Analysis of Dam-Reservoir Interaction in Time Domain, World Applied Sciences Journal, 15 (2011) 10, pp. 1403-1408

[17] Shariatmadar, H., Mirhaj, A.: Dam-reservoir-foundation interaction effects on the modal characteristic of concrete gravity dams, Structural Engineering and Mechanics, 38 (2011) 1, pp. 65-79

[18] Chen, B., Yuan, Y.: Hydrodynamic Pressures on Arch Dam during Earthquakes, Journal of Hydraulic Engineering, 137 (2011).1, pp. 34-44

[19] Wang, H., Feng, M., Yang, H.: Seismic nonlinear analyses of a concrete gravity dam with 3D full dam model, Bullettin of Earthquake Engineering, 10 (2012) 6, pp. 1959-1977

[20] Lin, G., Wang, Y., Hu, Z.: An efficient approach for frequency-domain and time-domain hydrodynamic analysis of dam–reservoir systems, Earthquake Engineerıng and structural Dynamics, 41 (2012) 13, pp. 1725-1749

[21] Miquel, B., Bouaanani, N.: Accounting for Earthquake-Induced Dam-Reservoir Interaction Using Modified Accelerograms, Journal of Hydraulic Engineering, 139 (2013) 9, pp. 1608-1617

[22] Samii, A., Lotfi, V.: A high order based boundary condition for dynamic analysis of infinite reservoirs, Computers and Structures, 120 (2013), pp. 65-76

[23] Wick, T.: Coupling of fully Eulerian and arbitrary Lagrangian-Eulerian methods for fluid-structure interaction computations, Computational Mechanics, 52 (2013) 5, pp. 1113–1124

[24] Yahyai, M., Rezayibana, B., Mohammadrezapour, E.: Effect of near-fault earthquakes with forward directivity on telecommunication towers, Earthquake Engineering and Engineering Vibration, 10 (2011) 2, pp. 211-218

[25] Agrawal, A.K., He, W.L.: A closed-form approximation of near-fault ground motion pulses for flexible structures, Proceedings of the 15th ASCE engineering mechanics conference, New York, 2002.

[26] Somerville, P.G.: Magnitude scaling of the near-fault rupture directivity pulse, Phys. Earth Planet. Inter., 137 (2003), pp. 201-212

[27] Akkar, S., Yazgan, U., Gulkan, P.: Drift estimates in frame buildings subjected to near-fault ground motions, Journal of Structural Engineering ASCE, 131 (2005), pp. 1014-1024

[28] Adanur, S., Altunişik, A.C., Bayraktar, A., Akköse, M.: Comparison of near-fault and far-fault ground motion effects on geometrically nonlinear earthquake behavior of suspension bridges, Natural Hazards, 64(2012), pp. 593-614

[29] Bray, J.D., Rodriguez-Marek, A.: Characterization of forward-directivity ground motions in the near-fault region, Soil Dynamics and Earthquake Engineering, 24 (2004) 11, pp. 815-828

[30] Chopra, A.K., Chintanapakdee, C.: Comparing response of SDF systems to near-fault and far-fault earthquake motions in the context of spectral regions, Earthquake Engineering and Structural Dynamics, 30 (2001), pp. 1769-1789

[31] Bayraktar, A., Altunişik, A.C., Sevim, B., Ates, S.: Effects of Pulse Signal of Near-Fault Strong Ground Motion on Nonlinear Response of Concrete Gravity Dam-Reservoir-Foundation, Proceedings of the International Symp. On Advances in Earthquake & Structural Engineering, Süleyman Demirel University, Isparta-Antalya, Turkey, 2007.

[32] Hall, J.F., Heaton, T.H., Halling, M.W., Wald, D.J.: Near-Source Ground Motion and its Effects on Flexible Buildings, Earthquake Spectra, 11 (1995) 4, pp. 569-605

[33] Malhotra, P.K.: Response of buildings to near-field pulse-like ground motions, Eartquake Engineering and Structural Dynamics, 28 (1999), pp. 1309-1326

[34] Alavi, B., Krawinkler, H.: Consideration of near-fault ground motion effects in seismic design, Proceedings of the 12th World Conference of Earthquake Engineering, New Zealand, 2000., Paper No. 2665

[35] MacRae, G.A., Mattheis, J.: Three-dimensional steel building response to near-fault motions, Journal of Structural Engineering, 126 (2000), pp. 117-126

[36] Alavi, B., Krawinkler, H.: Strengthening of moment-resisting frame structures against near-fault ground motion effects, Earthquake Engineering and Structural Dynamics, 33 (2004), pp. 707-722

[37] Liao, W.L., Loh, C., Lee, B.: Comparison of dynamic response of isolated and non-isolated continuous girder bridges subjected to near-fault ground motions, Engineering Structures, 26 (2004), pp. 2173-2183

[38] Shen, J., Tsai, M., Chang, K., Lee, G.C.: Performance of a Seismically Isolated Bridge under Near-Fault Earthquake Ground Motions, Journal of Structural Engineering, 130 (2004) 6, pp. 861-868

[39] Yan, X., Lee, G.C.: Traveling wave effect on the seismic response of a steel arch bridge subjected to near fault ground motions, Earthquake Engineering and Engineering Vibration, 6 (2007) 3, pp. 245-257

[40] Prtidakis, C.P.: Pushover analysis of base isolated steel concrete composite structures under near fault excitations, Soil Dynamics and Earthquake Engineering, 28 (2007), pp. 293-304

[41] Phan, V., Saiidi, M.S., Anderson, J., Ghasemi, H.: Near-fault ground motion effects on reinforced concrete bridge columns, Journal of Structural Engineering, 133 (2007) 7, pp. 982-989

[42] Su, C., Sung, Y., Chang, S., Huang, C.: Analytical investigations of seismic responses for reinforced concrete bridge columns subjected to strong near-fault ground motion, Earthquake Engineering and Engineering Vibration, 6 (2007) 3, pp. 237-244

[43] Jonsson, M.H., Bessason, B., Haflidason, E.: Earthquake response of a base-isolated bridge subjected to strong near-fault ground motion, Soil Dynamics and Earthquake Engineering, 30 (2010), pp. 447-455

[44] Corigliano, M., Scandella, L.: Seismic analysis of deep tunnels in near fault conditions in Southern Italy as case study, Bullettin of Earthquake Engineering, 9 (2011), pp. 975-995

[45] Karalar, M., Padgett, J.E., Dicleli, M.: Parametric analysis of optimum isolator properties for bridges susceptible to near-fault ground motions, Engineering Structures, 40 (2012), pp. 276-287

[46] Amiri, F.S., Amiri, G.G., Razeghi, H.: Estimation seismic demands of steel frames subjected to near-fault earthquakes having forward directivity and comparing with pushover analysis results, The Structural Design of Tall and Special Buildings, 22 (2013), pp. 975-988

[47] Panchal, V.R., Jangid, R.S.: Behaviour of liquid storage tanks with variable curvature friction pendulum system (VCFPS) under near-fault ground motions, Structure and Infrastructure Engineering, 8 (2014) 1, pp. 71-88

[48] Gang, W., Changhai, Z., Shuang, L., Lili, X.: Effects of near-fault ground motions and equivalent pulses on Large Crossing Transmission Tower-line System, Engineering Structures, 77 (2014), pp. 161-169

[49] Antonellis, G., Panagiotou, M.: Seismic response of bridges with rocking foundations compared to fixed-base bridges at near-fault site, Journal of Bridge Engineering, 19 (2014) 5.

[50] Wilson, E.L., Khalvati, M.: Finite elements for the dynamic analysis of fluid-solid systems, International Journal for Numerical Methods in Engineering, 19 (1983) 11, pp. 1657-1668

[51] Bathe, K.J.: Finite Element Procedures in Engineering Analysis, Englewood Cliffs, New Jersey, Prentice-Hall, 1996.

[52] Clough, R.W., Penzien, J.: Dynamics of Structures, McGraw-Hill, New York, USA, 1975.

[53] Akkaş, N., Akay, H.U., Yılmaz, C.: Applicability of general-purpose finite element programs in solid-fluid interaction problems, Computers and Structures, 10 (1979) 5, pp. 773-783

[54] Cook, R.D., Malkus, D.S., Plesha, M.E.: Concept and Applications of Finite Element Analysis, John Wiley and Sons, Singapore, 1989.

[55] Zeinkiewicz, O.C., Taylor, R.L.: Finite Element Method, McGraw-Hill, London, 1991.

[56] Pacific Earthquake Engineering Research Centre: http://ngawest2.berkeley.edu, 1.12. 2015.

[57] Ghanaat, Y.: Seismic performance and damage criteria for concrete dams, Proceedings of the 3rd US-Japan Workshop on Advanced Research on Earthquake Engineering for Dams, San Diego, California, USA, 2002.

[58] USACE: Time-History Dynamic Analysis of Concrete Hydraulic Structures, Engineering and Design, EM 1110-2-6051, USA, 2003.